GEORG-AUGUST-UNIVERSITÄT GÖTTINGEN

Fakultät für Physik

Master's Thesis

Durch Kolloide hervorgerufene Defekte in smektischen Flüssigkristallen

Colloid-induced topological defects in smectic liquid crystals

prepared by

Victor Meiwes Turrión

from Göttingen

at the Max Planck Institute for Dynamics und Self-Organisation
Department for Dynamics of Complex Fluids

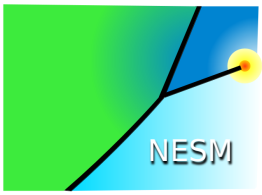

Thesis period: 26th May 2016 until 23rd November 2016

First Rreferee: Dr. Marco G. Mazza

Second referee: Prof. Dr. Marcus Müller

Contents

1 List of publications

S. Püschel-Schlotthauer, V. Meiwes Turrión T. Stieger, R. Grotjahn, C. K. Hall, M. G. Mazza, M. Schoen, The Journal of Chemical Physics **145**, 164903 (2016)

S. Püschel-Schlotthauer, V. Meiwes Turrión, C. K. Hall, M. G. Mazza, M. Schoen, Langmuir (2016), under review

2 Introduction

Liquid crystals (LC) are fascinating materials which can often be found to be visually pleasing and which exhibit an anisotropy in some of their macroscopic properties such as for example in their refractive index or electric and magnetic susceptibility [1]. Due to these properties, they are of interest for various practical applications [2–4]; presently the most prominent one, of course, being LC displays (LCDs). Embedding microscopic particles, such as colloids, in a LC can result in self-organization of the inclusions into chains, crystals or quasi-crystals [5–8].

The macroscopic anisotropy of LC can be traced back to the shape of its constituent molecules, which are non-polar and of anisotropic shape; most often either prolate or oblate. Most examples for LC molecules consist of organic molecules, e.g. the family of cyanobiphenyls [9] or some derivatives of cholesterol [10], even biological membranes can be understood as LCs. However, there are examples for non-organic LCs [11], also it is known that a system of hard rods can undergo an isotropic-nematic phase transition [1, 12, 13].

Due to their anisotropic shape, the molecules of LCs posses orientational degrees of freedom in addition to their spatial degrees of freedom. Whereas systems of isotropic particles can only display various states of different spatial order (e.g. crystalline with long-range correlations of positions, or fluid with short range correlations of positions), LC molecules can additionally exhibit long-range orientational order. Combining spatial and orientational order and considering different shapes of molecules, results in a variety of ordered states. The simplest of these LC states is the nematic state, in which the molecules are spatially ordered like a liquid but aligned along a common axis. Smectic phases are similar to the nematic phase, in that all molecules are aligned along a common axis. However, spatially the translational symmetry of a liquid is broken in one dimension, as the molecules are arranged into layers. Within the layers, the molecules only exhibit short range positional order, thereby resembling a two-dimensional liquid.

Being ordered media, LCs with long ranged orientational order can exhibit topo-

logical defects. These are sets of points on which the local orientation of the LC becomes singular, and which cannot be eliminated, by continuously deforming the surrounding orientations. The theoretical treatment of ordered media and their defects is deeply connected with the theory of homotopy groups [14]. In nematic LCs, these defects consist of either single points or of lines, also referred to as disclinations. Defects in nematic LCs bear some similarity to elementary particles; a notion of charge can be defined for these defects, defects with charge of the same sign repel each other, whereas defects with charges of opposing sign attract each other [15]. Furthermore, defects of opposing charge can annihilate one another if they get close enough [15]. The presence of a topological defect can influence the director field even far away from the actual singularity, and they play an important role in the interactions of inclusions in a nematic host phase [16].

For smectic LCs extensive experimental and theoretical work has been done for various aspects of this type of LC phase [6, 17–20]. Yet, there are only few studies examining smectic LCs by means of numerical tools. This thesis aims to contribute in closing this gap. We present results of molecular dynamics simulations for a simple LC model, capable of forming a nematic and a smectic A phase. Bulk properties of the model are examined, such as its self-diffusion and its elastic constants. Furthermore, we investigate the effects of colloidal inclusions and the formation of topological defects in the nematic and in the smectic A phase, in an effort to asses whether this simple model can capture properties, found experimentally by Zuhail et al. [6, 21, 22].

3 Theory

3.1 Liquid crystals

A liquid crystal (LC) is a material consisting of anisotropic, head-tail symmetric molecules, i.e., they can be approximated by either rod-like or disc-like objects. The anisotropy of their constituents is essential for the microscopic order of LCs as well as for their macroscopic properties. Molecules characterized by isotropic interactions, such as nitrogen, display three different states of aggregation: a solid, a liquid and a gaseous state. Microscopically, these phases are distinguished by the spatial order of the molecules. In the solid phase, the molecules' positions are correlated, and thus ordered, over long distances as they are arranged on a periodic lattice. This long-range order is absent in the liquid and in the gaseous phase. In the liquid phase the molecules' positions are still correlated over short distances, but even these short-ranged correlations practically vanish in the gaseous phase. LC particles posses, additionally to their spatial degrees of freedom, orientational degree of freedom in which order may be found. The combination of spatial and orientational correlations leads to a rich variety of different phases, ranging from a perfectly ordered crystal to an isotropic gas, with many phases of different, intermediate kinds of order (see Figure 3.1).

Perhaps the simplest of these intermediate phases is the nematic phase. Similar to the case of an ordinary liquid, the centers of mass of the LC particles are spatially disordered in this phase. However, the long axes of the LC particles are aligned along a common axis and are thus highly ordered. The unit vector $\hat{\mathbf{n}}$ parallel to this axis is denoted as the nematic director; a more explicit definition is given below. Macroscopically, the orientational anisotropy can manifest itself in the form of direction-dependent refractive indices and polarizing capabilities of the nematic material or anisotropic flow behavior.

In a smectic phase, the LC centers of mass are arranged in equidistant, parallel layers, similar to books in a bookshelf. Within these layers, however, the particles

only show short range positional order. This phase can be seen as a combination of a one-dimensional crystal with a two-dimensional liquid. The LC particles' orientations are ordered, like in the nematic phase. Different classes of smectic phases can be distinguished by the relative orientation of the director to the layers' normal. In case the director and the layers' normal are parallel to each other, the phase is denoted as smectic A; if they are tilted with respect to each other, the phase is referred to as smectic C. Only the former will be of importance in the present thesis.

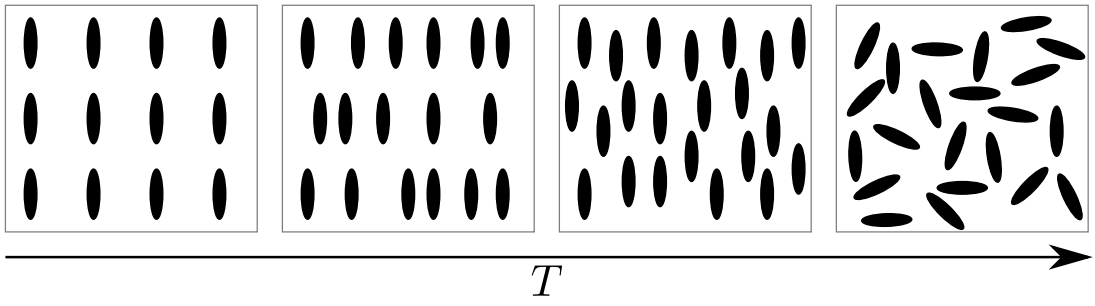

Figure 3.1: Sketches of different phases of calamitic LCs. From left to right: crystalline phase, smectic A phase, nematic phase, isotropic phase.

Other LC phases include columnar phases, chiral or cholesteric phases, and blue phases. These phases shall only be mentioned by name, as they do not appear in the studied model.

3.1.1 Nematic liquid crystals

In a nematic LC, the positions of the LC particles are disordered, similar to the molecules of a liquid, whereas their orientations are highly ordered. Generally, two types of nematic phases can be distinguished from each other: uniaxial and biaxial phases. Systems of the latter phase have three distinguished axes, along which certain macroscopic quantities[1] differ from each other. Therefore, these systems are invariant under two-fold rotations, which map these axes onto themselves. Uniaxial systems on the other hand, posses only one distinguished axis, making them invariant under continuous rotations around this axis. Microscopically, these differences can be traced back to the shape of the constituent LC particles, which approximately mirror the macroscopic symmetries. In the context of the present thesis, the considered LCs form only uniaxial phases, as their molecules are modeled as prolate particles.

[1] The refractive index is the quantity which is most commonly considered in real systems, but other quantities such as diffusion coefficients or one-dimensional radial distribution functions could possibly also be considered.

Nematic order parameter and director

In order to quantify the amount of orientational order of a LC, an order parameter is needed. The symmetry of a uniaxial nematic fluid is clearly described by one direction. However, because of the head-tail symmetry of the molecules, a vector does not truly represent the state of the system, as a vector $\mathbf{v}$ is not invariant under parity, $\mathbf{v} \to -\mathbf{v}$. The next geometric object of higher order is a rank-2 tensor. We will see below, that it is possible to find a scalar order parameter from an invariant of the tensor order parameter. By convention, the scalar nematic order parameter S is required to be one for a nematic system with perfect orientational order and to vanish for an isotropic system. For the construction of such a scalar, a system of N LC particles is considered. Let $\hat{\mathbf{u}}_n$ denote the orientation of the n-th particle, and let u_{in} refer to its component along the i-th Cartesian coordinate axis ($i \in \{1, 2, 3\}$). All orientations $\hat{\mathbf{u}}$ lie on the unit sphere $\mathcal{S}^2$, i.e. $\|\hat{\mathbf{u}}\| = 1$, where $\|\cdot\|$ denotes the Euclidean norm. Using this notation, the nematic order tensor $\mathbf{Q}$ is defined as

$$\mathbf{Q} \equiv \frac{1}{2N} \sum_{n=1}^{N} \left(3\hat{\mathbf{u}}_n \otimes \hat{\mathbf{u}}_n - \mathbf{1}\right), \tag{3.1}$$

where $\otimes$ refers to the tensor product, and $\mathbf{1}$ is the unit tensor. Note that $\mathbf{Q}$ captures the head-tail symmetry of the LC particles. As can be seen from the definition, the tensor $\mathbf{Q}$ can be represented as a real, symmetric, traceless 3×3 matrix and as such it is diagonalizable and has up to three different, real eigenvalues. As it turns out, two of its eigenvalues are always degenerate, and the third eigenvalue lies between zero and one, depending on whether all LC particles are oriented parallel to each other or not. Therefore, this third eigenvalue is an appropriate quantity to function as the order parameter S. The unit vector $\hat{\mathbf{n}}$, associated to the third eigenvalue is denoted as the global director of the system and corresponds roughly to the average direction along which the LC particles are oriented. It should be noted that the director $\hat{\mathbf{n}}$ is physically equivalent to its negative $-\hat{\mathbf{n}}$ because of the head-tail symmetry of the molecules.

3.1.2 Eigenvalues of the nematic order tensor Q

In the following, the possible eigenvalues of the nematic order tensor $\mathbf{Q}$ are discussed. For this purpose the orientation vector $\hat{\mathbf{u}}$ will be written in spherical coordinates

$$\hat{\mathbf{u}} = \begin{pmatrix} u_1 \\ u_2 \\ u_3 \end{pmatrix} = \begin{pmatrix} \sin(\theta)\cos(\phi) \\ \sin(\theta)\sin(\phi) \\ \cos(\theta) \end{pmatrix}, \tag{3.2}$$

where $\theta \in [0, \pi]$ denotes the polar angle and $\phi \in [0, 2\pi]$ denotes the azimuthal angle. Consider now a uniaxial nematic system where the orientation $\hat{\mathbf{u}}$ of each particle is distributed according to the probability distribution function $\varrho(\phi, \theta)$. Due to uniaxiality, the probability distribution function ϱ is invariant under rotations around the

nematic director. By choosing the coordinate system such that the director coincides with the third coordinate axis, the distribution ϱ becomes independent of the azimuthal angle ϕ ($\varrho(\theta) \equiv \varrho(\phi, \theta)$). Furthermore, ϱ must also be symmetric around $\theta = \pi/2$ because of the head-tail symmetry of the LC particles, however, this property will be of no importance for the following calculations. It is straightforward to calculate the expected value of the outer product $\hat{\mathbf{u}} \otimes \hat{\mathbf{u}}$ in this coordinate system; its components $u_i u_j$ are given by

$$\langle u_1 u_2 \rangle = \underbrace{\int_0^{2\pi} \cos(\phi) \sin(\phi) \, \mathrm{d}\phi}_{=0} \int_0^{\pi} \sin(\theta)^2 \varrho(\theta) \, \mathrm{d}\theta = 0 \tag{3.3}$$

$$\langle u_1 u_3 \rangle = \underbrace{\int_0^{2\pi} \cos(\phi) \, \mathrm{d}\phi}_{=0} \int_0^{\pi} \sin(\theta) \cos(\theta) \varrho(\theta) \, \mathrm{d}\theta = 0 \tag{3.4}$$

$$\langle u_2 u_3 \rangle = \underbrace{\int_0^{2\pi} \sin(\phi) \, \mathrm{d}\phi}_{=0} \int_0^{\pi} \sin(\theta) \cos(\theta) \varrho(\theta) \, \mathrm{d}\theta = 0 \tag{3.5}$$

$$\langle u_1 u_1 \rangle = \underbrace{\int_0^{2\pi} \cos(\phi)^2 \, \mathrm{d}\phi}_{=\pi} \int_0^{\pi} \sin(\theta)^2 \varrho(\theta) \, \mathrm{d}\theta \equiv \alpha \tag{3.6}$$

$$\leq \pi \int_0^{\pi} \varrho(\theta) \, \mathrm{d}\theta = \frac{1}{2}$$

$$\langle u_2 u_2 \rangle = \underbrace{\int_0^{2\pi} \sin(\phi)^2 \, \mathrm{d}\phi}_{=\pi} \int_0^{\pi} \sin(\theta)^2 \varrho(\theta) \, \mathrm{d}\theta = \alpha \tag{3.7}$$

$$\langle u_3 u_3 \rangle = \underbrace{\int_0^{2\pi} \mathrm{d}\phi}_{=2\pi} \int_0^{\pi} \cos(\theta)^2 \varrho(\theta) \, \mathrm{d}\theta = 1 - 2\alpha. \tag{3.8}$$

In this coordinate system $\hat{\mathbf{u}} \otimes \hat{\mathbf{u}}$ is already diagonal: $\hat{\mathbf{u}} \otimes \hat{\mathbf{u}} = \mathrm{diag}(\alpha, \alpha, 1 - 2\alpha)$, where $\alpha \in [0, 1/2]$. Three different extreme cases for the distribution ϱ of the orientations $\hat{\mathbf{u}}$ can be considered. In the first case the orientations $\hat{\mathbf{u}}$ are distributed uniformly on the unit sphere, which corresponds to an isotropic state. Therefore, the distribution ϱ is proportional to $\sin(\theta)$, which is just the Jacobian determinant for the transformation of Cartesian to spherical coordinates for radii $r = 1$. In this

case the tensor product $\hat{\mathbf{u}} \otimes \hat{\mathbf{u}}$ becomes diag $(1/3, 1/3, 1/3)$. The second extreme case is a perfect nematic state, in which all orientations $\hat{\mathbf{u}}$ are aligned along the third coordinate axis. In this case the distribution ϱ should be proportional to $(\delta(\theta) + \delta(\theta - \pi))$, with δ referring to the Dirac delta distribution, and the tensor product $\hat{\mathbf{u}} \otimes \hat{\mathbf{u}}$ becomes diag $(0, 0, 1)$. In the last extreme case, all orientations $\hat{u}$ are aligned parallel to the same plane but show no preferred orientation otherwise; the distribution ϱ is proportional to $\delta(\theta - \pi/2)$ and the outer product $\hat{\mathbf{u}} \otimes \hat{\mathbf{u}}$ becomes diag $(1/2, 1/2, 0)$. This case neither corresponds to a truly isotropic nor to a nematic state.

When considering systems of particles, one expects the distribution ϱ of orientations $\hat{\mathbf{u}}$ to lie somewhere between the isotropic and the nematic case, meaning that, if ϱ has a single local maximum at $\theta = \pi/2$, the peak should not be sharper than $\sin(\theta)$. For this range of cases, $\hat{\mathbf{u}} \otimes \hat{\mathbf{u}}$ always has one large eigenvalue λ_0 and two smaller ones $\lambda_{1,2}$ (except in the case of an isotropic state). The magnitude of the large eigenvalue gives a measure for how nematic the system is, since the magnitude grows with increasing "nematicity". This gives some motivation to use $\hat{\mathbf{u}} \otimes \hat{\mathbf{u}}$ for the construction of the nematic order parameter since its largest eigenvalue is minimal in the isotropic phase ($\lambda_0 = 1/3$) and maximal in the nematic phase ($\lambda_0 = 1$).

3.1.3 Landau-de Gennes theory

The isotropic nematic (IN) phase transition can be studied phenomenologically, parting from the general framework of Landau [23], which he developed to describe temperature-driven phase transitions. De Gennes adapted this theory for the IN transition of a uniaxial system [1]. For that he assumed that the scalar nematic order parameter S is small in the nematic phase, close to the nematic smectic transition. Therefore the free energy F of the system can be expanded in the order parameter. Truncating the expansion at the term of fourth order, the free energy F takes on the form

$$F(S) = \frac{3}{4} A(T) S^2 - \frac{1}{4} B(T) S^3 + \frac{9}{16} C(T) S^4 \tag{3.9}$$

where the expansion coefficients A, B and C are generally temperature dependent and a priori unknown. The third order term is required to vanish in order to ensure, that the free energy F always exhibits a local minimum for the isotropic state ($S = 0$) and it also results in the phase transition being of first order. It can be assumed, that the coefficients B and C are practically temperature indepent close to the phase transition and that A is roughly proportional to $(T - T^*)$, where T^* is the temperature of the spinodal. This assumption is in agreement with molecular theories [1]. With these coefficients, the free energy F behaves qualitatively differently, depending on the temperature T as shown in Figure 3.2.

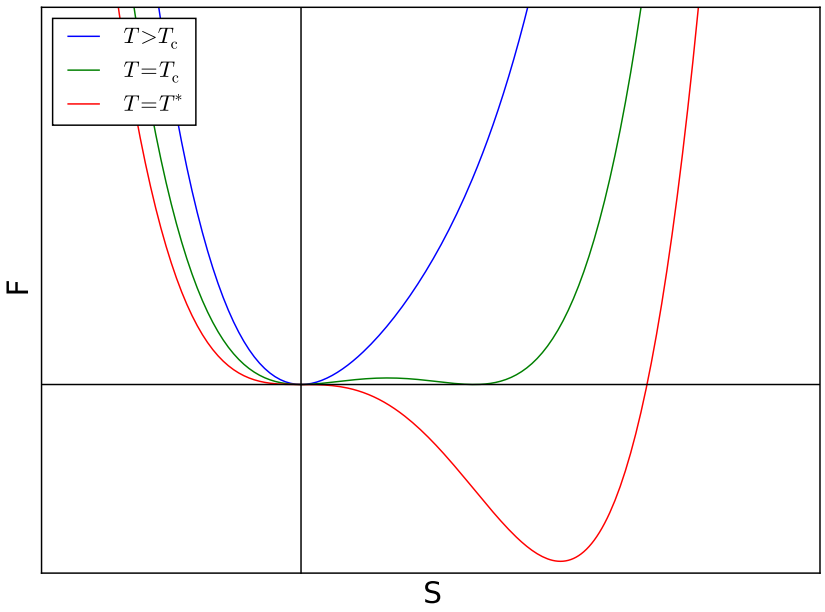

Figure 3.2: The free energy depending on the nematic order parmeter S for different temperatures T. For $T > T_c$ the global minimum of the free energy F is located at $S = 0$, corresponding to an isotropic state. For $T < T_c$ the absolute minimum of F corresponds to a nematic state with $S \neq 0$ and at $T = T_c$ there can be phase coexistence. For temperature below T^* the isotropic phase with $S = 0$ becomes completely unstable.

3.1.4 Smectic liquid crystals

Just like in nematic phases, the orientations of the LC particles in a smectic phase are highly ordered. But in contrast to the former phase, the particles in a smectic phase are arranged in equidistant layers, thus being spatially ordered in one dimension. Within the layers, however, the particles behave like a fluid. The term smectic encompasses several phases, which all share the order described above, but which are qualitatively different. One of these phases is called smectic A. In this phase, the director $\hat{\mathbf{n}}$ is parallel to the layers' normal $\hat{\mathbf{p}}$. In the phases denoted by smectic C, the director $\hat{\mathbf{n}}$ is tilted away from the layers' normal $\hat{\mathbf{p}}$. This tilt makes smectic C systems biaxial, whereas smectic A systems are uniaxial. Also, when considering inclusions embedded in a smectic C system, the head-tail symmetry of the director field is broken. The smectic systems treated in this thesis are only smectic A.

For the construction of an order parameter Λ which quantifies the spatial ordering into layers, consider a system of volume V containing N LC particles and let $\rho(\mathbf{x})$ denote the normalized particle density at position $\mathbf{x}$. In the case of a layered arrangement of the particles, the density exhibits a periodic modulation along the layers normal, with the period being the inter-layer distance d. The order parameter

Λ can be defined as the first harmonic of this modulation [1, 24]. For an explicit expression, consider the Fourier transform of the normalized density ρ along the layer normal, which coincides with the director $\hat{\mathbf{n}}$ in a smectic A system

$$\hat{\rho}(k) = \int_V \rho(\mathbf{x})\, e^{-i2\pi k(\hat{\mathbf{n}}\cdot\mathbf{x})} \mathrm{d}^3x. \tag{3.10}$$

The order paramter Λ is then given by its amplitude at the inverse inter-layer distance $k_0 = 1/d$

$$\Lambda = |\hat{\rho}(k_0)| = \left(\hat{\rho}^*(k_0)\,\hat{\rho}(k_0)\right)^{\frac{1}{2}}, \tag{3.11}$$

where $\hat{\rho}^*$ denotes the complex conjugate of $\hat{\rho}$.

This is a valid choice for the smectic order parameter, since in the case of a spatially homogeneous system the normalized particle density $\rho(\mathbf{x})$ would be just the constant $1/V$. Its Fourier transform $\hat{\rho}$ would thus be proportional to $\delta(k)$, such that $\Lambda = 0$ for wave numbers $k \neq 0$. On the other hand, if the all particles were perfectly aligned on layers the density ρ would be given by $\rho(\hat{\mathbf{x}}) = 1/N \sum_n \delta(\mathbf{x} - \mathbf{x}_n)$ such that $\hat{\mathbf{n}}\cdot\mathbf{x}_n = m_n d + \omega$ where m_n is an integer describing the layer in which particle n is located and ω is the offset of the zeroth layer. In that case the Fourier transform $\hat{\rho}$ would be given by $\hat{\rho}(k) = 1/N \sum_n \exp(-i2\pi k d m_n + i\phi)$ with integer numbers m_n and consequently $\Lambda = 1$. The layer spacing d can also be extracted from $\hat{\rho}$, in case that the former is not known beforehand, by looking for local maxima of $\hat{\rho}$ as the number k is varied.

3.2 Models for LCs

3.2.1 Hess-Su model

A relatively simple and quite general model for LCs has been introduced by Hess and Su [25] based on an isotropic pair potential U_{HS} for LC particles. In this model, the LC particles n are described by the position of their center of mass $\mathbf{x}_n$, and their orientation described by a unit vector $\hat{\mathbf{u}}_n$. The pair potential is given by

$$U_{\mathrm{HS}}(\mathbf{r}_{ij}, \hat{\mathbf{u}}_i, \hat{\mathbf{u}}_j) = 4\epsilon_0 \left[\left(\frac{\sigma}{r_{ij}}\right)^{12} - \left(\frac{\sigma}{r_{ij}}\right)^{6} \left(1 + \Psi(\hat{\mathbf{r}}_{ij}, \hat{\mathbf{u}}_i, \hat{\mathbf{u}}_j)\right) \right] \tag{3.12}$$

where the vector $\mathbf{r}_{ij} \equiv (\mathbf{x}_j - \mathbf{x}_i)$ points from particle i to particle j and r_{ij} denotes its length. The anisotropy of the potential enters via the factor Ψ. Disregarding this factor, the remaining isotropic part of the potential is just the Lennard-Jones potential [26]. As such, the energy ϵ_0 corresponds to the potential's value at its local minimum located at $r_{ij} = 2^{1/6}\sigma$. Expressions for the anisotropic factor Ψ can be obtained by expanding the attractive part of the potential (the leading term in the far field) in rotational invariants [27]

$$\Psi(\hat{\mathbf{r}}_{ij}, \hat{\mathbf{u}}_i, \hat{\mathbf{u}}_j) = \epsilon_1\Phi_{220} + \epsilon_2\left[\Phi_{202} + \Phi_{022}\right] + \epsilon_3\Phi_{222} + \epsilon_4\Phi_{440} + \epsilon_5\Phi_{224} \tag{3.13}$$

$$\text{with} \quad \Phi_{l_i,l_j,l}\left(\hat{\mathbf{u}}_i,\hat{\mathbf{u}}_j,\hat{\mathbf{r}}_{ij},\right) \equiv \sum_{m_i,m_j,m} \langle l_i,l_j,m_i,m_j|lm\rangle \times \mathcal{Y}_{l_i}^{m_i}\left(\omega(\hat{\mathbf{u}}_i)\right)\mathcal{Y}_{l_j}^{m_j}\left(\omega(\hat{\mathbf{u}}_j)\right)\mathcal{Y}_{l}^{m*}\left(\omega(\hat{\mathbf{r}}_{ij})\right) \tag{3.14}$$

The expression within angular brackets is a Clebsch-Gordan coefficient and the functions $\mathcal{Y}$ are spherical harmonics with the superscript $*$ denoting their complex conjugate. The expression $\omega(\hat{\mathbf{u}}_n) \equiv (\Theta_n, \phi_n)$ is used to refer to the polar and azimuthal angle of a unit vector $\hat{\mathbf{u}}_n$. By only admitting invariants Φ_{klm} with even numbers k,l and m, the head-tail symmetry of the LC particles is assured. The parameters ϵ_1 through ϵ_5 are the strengths of the potential's corresponding multipole moments and can in principle be chosen freely. By selecting appropriate parameter values, it is possible to model non-chiral LC particles of a large variety of shapes. For modeling simple nematic LC it is sufficient to consider only the parameters ϵ_1 and ϵ_2, and setting the remaining parameters equal to zero [25, 27]. In this case, the anisotropic factor is explicitly given by

$$\psi\left(\hat{\mathbf{r}}_{ij},\hat{\mathbf{u}}_i,\hat{\mathbf{u}}_j\right) = 5\epsilon_1 P_2\left(\hat{\mathbf{u}}_i\cdot\hat{\mathbf{u}}_j\right) + 5\epsilon_2\left[P_2\left(\hat{\mathbf{u}}_i\cdot\hat{\mathbf{u}}_{ij}\right) + P_2\left(\hat{\mathbf{u}}_j\cdot\hat{\mathbf{u}}_{ij}\right)\right], \tag{3.15}$$

where $P_2(x) \equiv 1/2(3x^2-1)$ denotes the second Legendre polynomial.

3.2.2 Modified model for smectic LCs

The LC model studied in this thesis uses a pair potential which is constructed similarly to the potential U_{HS}. But instead of the Lennard-Jones potential, the isotropic part of the potential is given by a repulsive part which is proportional to r_{ij}^{-10} and an attractive part, shaped like a Yukawa potential

$$U_{\mathrm{mm}}\left(\mathbf{r}_{ij},\hat{\mathbf{u}}_i,\hat{\mathbf{u}}_j\right) = \epsilon_0\left[a\left(\frac{\sigma}{r_{ij}}\right)^{10} - b\frac{e^{-\eta r_{ij}}}{r_{ij}}\left(1+\Psi\left(\hat{\mathbf{r}}_{ij},\hat{\mathbf{u}}_i,\hat{\mathbf{u}}_j\right)\right)\right], \tag{3.16}$$

$$a = \frac{1}{10}\frac{1+\eta\sigma}{9-\eta\sigma}, \quad b = \sigma\frac{e^{\eta\sigma}}{9-\eta\sigma} \quad . \tag{3.17}$$

This choice for parameters a and b guarantees that the isotropic part of the potential exhibits a local minimum at the distance $r_{ij} = \sigma$, regardless of the value of η, and that the depth of that minimum is given by $-10^{-1}\epsilon_0$. The inverse screening length η influences the range and the steepness of the attractive part of the potential. This model uses the same anisotropy factor Ψ as given in equation (3.15). After testing of various values for parameters η, ϵ_1 and ϵ_2, we settled with the values $\eta = 3\sigma^{-1}$ and $2\epsilon_1 = -\epsilon_2 = 0.8\epsilon_0$ as simulations with this pair of values resulted in both nematic and smectic A phases. A contour plot of the potential with these parameter values is shown in Figure 3.3. Compared to the pair potential U_{HS} however, the potential (3.16) has the drawback of beeing computationally more expensive, as it requires the computation of an exponential function and the computation of a square root, when calculating the distance r_{ij}.

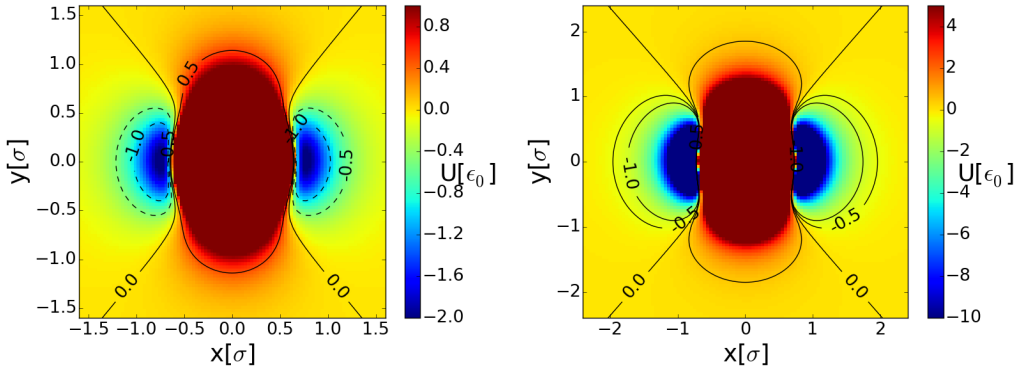

Figure 3.3: Left: contour plot of the potential (3.16) for $2\epsilon_1 = -\epsilon_2 = 0.8$ and $\hat{\mathbf{u}}_i = \hat{\mathbf{u}}_j = (0, 1, 0)$. Right: contour plot of the potential proposed by Hess-Su for $2\epsilon_1 = -\epsilon_2 = 0.8$ and $\hat{\mathbf{u}}_i = \hat{\mathbf{u}}_j = (0, 1, 0)$; here the numerical value of ϵ_0 is set to $\epsilon_0 = 0.1$ in order for the minima of both potentials to lie within the same order of magnitude.

3.2.3 Constraints on parameters ϵ_1,ϵ_2

Depending on the parameters ϵ_1 and ϵ_2 the potentials given by equation (3.12) or by equation (3.16) produce different interactionsand favour different pair configurations of LC particles. Also, the geometry of the potentials' surfaces of equal energy depends on those parameters, resulting in LC particles which can effectively be either prolate, oblate or spherical. But not every parameter combination ends up generating LC phases, let alone smectic phases. In an attempt to reduce the amount of admissible pairs of ϵ_1 and ϵ_2 a heuristic hierarchy was considered on the energy hierarchy of different extremal configurations. For two particles i and j these extremal configurations are the side-by-side configuration ($\hat{\mathbf{u}}_i \cdot \hat{\mathbf{u}}_j = 1$, $\hat{\mathbf{u}}_i \cdot \hat{\mathbf{r}}_{ij} = \hat{\mathbf{u}}_j \cdot \hat{\mathbf{r}}_{ij} = 0$), the end-to-end configuration ($\hat{\mathbf{u}}_i \cdot \hat{\mathbf{u}}_j = \hat{\mathbf{u}}_i \cdot \hat{\mathbf{r}}_{ij} = \hat{\mathbf{u}}_j \cdot \hat{\mathbf{r}}_{ij} = 1$), the X-shape configuration ($\hat{\mathbf{u}}_i \cdot \hat{\mathbf{u}}_j = \hat{\mathbf{u}}_i \cdot \hat{\mathbf{r}}_{ij} = \hat{\mathbf{u}}_j \cdot \hat{\mathbf{r}}_{ij} = 0$) and the T-shape configuration ($\hat{\mathbf{u}}_i \cdot \hat{\mathbf{u}}_j = 0$, $\hat{\mathbf{u}}_i \cdot \hat{\mathbf{r}}_{ij} = 1$, $\hat{\mathbf{u}}_j \cdot \hat{\mathbf{r}}_{ij} = 0$). It was assumed that in a smectic A phase the side-by-side configuration should be more favorable than any other configuration and should therefore have the lowest energy. The X-shape configuration should be less favorable, however, and it should still have lower energy than the end-to-end and the T-shape configuration. The latter of them is expected to be the least favorable of all configurations. This imposes an ordering of the anisotropy factors for the different configurations $\Psi_\mathrm{T} < \Psi_\mathrm{ee} < \Psi_\mathrm{X} < \Psi_\mathrm{ss}$, which in turn results in three constraints on the parameters ϵ_1 and ϵ_2

$$0 < \epsilon_1 \tag{3.18}$$

$$-\epsilon_1 < \epsilon_2 \tag{3.19}$$

$$\epsilon_2 < -\frac{1}{2}\epsilon_1 \tag{3.20}$$

A fourth constraint can be made using the assumption that the potential energy

of every configuration should have a local minimum. For the potential 3.12 this condition yields the inequality $\Psi+1>0$. Naively, one could insert $\Psi = 5(\epsilon_1/2+2\epsilon_2)$ for the lowest value of the factor Ψ. This value, however, is geometrically impossible, since both orientations $\hat{\mathbf{u}}_i$ and $\hat{\mathbf{u}}_j$ need to be orthogonal to each other while both being aligned along the connection vector $\mathbf{r}_{ij}$. Instead, using Ψ_T for the lowest possible value of the anisotropy factor Ψ results in the condition

$$\epsilon_1 - \frac{2}{5} < \epsilon_2. \tag{3.21}$$

These four conditions reduce the set of admissible parameters to a triangular domain in the ϵ_1-ϵ_2-plane as shown in Figure 3.4. (see Figure 3.4).

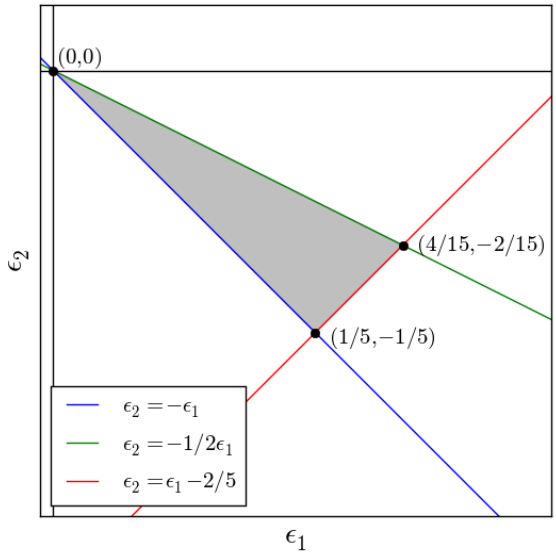

Figure 3.4: The conditions given by equations (3.18) through (3.21) limit the ranges of the parameters ϵ_1 and ϵ_2, which yield the desired hierarchy of U, to a triangle in the ϵ_1-ϵ_2-plane.

3.2.4 Condition for purely repulsive potential

Depending on the choice of the parameters ϵ_1 and ϵ_2 there may be configurations of particle pairs such that the inter-particle forces are purely repulsive. By requiring, that a certain orientational configuration ($\hat{\mathbf{u}}_i$, $\hat{\mathbf{u}}_j$, $\hat{\mathbf{r}}_{ij}$) should posses an equilibrium distance r, at which the forces between particle i and j vanish, yields the condition:

$$\partial_r U = \epsilon_0 \left[-10a\frac{\sigma^{10}}{r^{11}} + b\left(\eta + \frac{1}{r}\right)\frac{e^{-\eta r}}{r}\left(1+\Psi\right)\right] \stackrel{!}{=} 0 \tag{3.22}$$

$$\Leftrightarrow e^{\eta r} = \frac{b}{10a}\left(\frac{r}{\sigma}\right)^{10}\left(\eta + \frac{1}{r}\right)(1+\Psi) \tag{3.23}$$

$$\overset{\text{Eq.(3.17)}}{\Rightarrow} e^{\eta r} = \frac{e^{\eta\sigma}}{1+\eta\sigma}\frac{1+\Psi}{\sigma^9}(\eta r + 1)\, r^9 \tag{3.24}$$

$$\overset{\xi\equiv\eta r}{\Leftrightarrow} e^{\xi} = \underbrace{\frac{e^{\eta\sigma}}{1+\eta\sigma}\frac{1+\Psi}{\eta^9\sigma^9}}_{\equiv\alpha}(\xi+1)\,\xi^9 \tag{3.25}$$

$$\Rightarrow \frac{e^{\xi}}{\xi^{10}+\xi^9} \overset{!}{=} \alpha. \tag{3.26}$$

The constant α only depends on the choice of length scale σ, the parameters η, ϵ_1, ϵ_2 as well as the relations between the particle orientations $\hat{\mathbf{u}}_i$, $\hat{\mathbf{u}}_j$ and $\hat{\mathbf{r}}_{ij}$. The last expression cannot be solved in closed form, however, one can check for the existence of a solution. Since the variable ρ is a function of the inter-particle distance r, only solutions for positive values ρ need to be considered. For these cases the expression on the left hand side is always positive and it diverges at $\rho = 0$ and as ρ goes to infinity. Therefore, a local minimum must exist:

$$\frac{\partial}{\partial\xi}\left(\frac{e^{\xi}}{\xi^{10}+\xi^9}\right) \overset{!}{=} 0 \tag{3.27}$$

$$\Rightarrow \xi = \frac{9}{2} \pm \frac{3}{2}\sqrt{13}. \tag{3.28}$$

By choosing the positive solution for ρ and plugging it into equation (3.26), the value $\alpha_0 \approx 2.001569 \times 10^{-6}$ is found, which the number α has to exceed, if the corresponding orientational configuration is supposed to have an equilibrium distance. As it turns out, the end-to-end and the T-shape configurations are purely repulsive for the choice of $2\epsilon_1 = -\epsilon_2 = 0.8$, $\eta = 3\sigma^{-1}$. The values of α for the most relevant inter-particle configurations are listed as follows:

	side-side	X-shape	end-end	T-shape
α	0.0018	0.001	-0.001	-0.0005

3.2.5 Model interactions with walls and colloids

Not all simulations done in this thesis are performed with bulk systems. In some instances it is necessary to restrict the movement of the LC particles or to stabilize their alignment or both. For these purposes continuous walls are introduced parallel to the systems' x-y-plane. The interaction potential of each LC particle with the wall is given by

$$U_{\text{mw}}(z) = \epsilon_{\text{mw}}\left[\frac{1}{5}\left(\frac{\sigma}{z-z_{\text{w}}}\right)^{10} - \frac{1}{2}\left(\frac{\sigma}{z-z_{\text{w}}}\right)^{4} g(\hat{\mathbf{r}},\hat{\mathbf{u}})\right], \tag{3.29}$$

where z is the LC particle's coordinate, z_w the walls position along the third axis and ϵ_mw the walls energy-density per unit area. The anchoring function g modifies the attractive part of the potential, depending on the particles' orientations $\hat{\mathbf{u}}$, akin to the anisotropy factor Ψ in equation (3.16). In order to achieve homeotropic anchoring, aligning the LC particles at the wall along the x-axis, we choose g to be given by $g = (\hat{\mathbf{u}} \cdot \hat{\mathbf{e}}_x)^2$. For planar anchoring we chose the anchoring function to be given by $g = (1 - \hat{\mathbf{u}} \cdot \hat{\mathbf{e}}_x)^2$. In both cases the value of the energy scale is chosen to be $\epsilon_\mathrm{mw} = 10\epsilon_0$. The form of this potential is motivated by approximating the wall with a homogeneous distribution of particles, which interact with the LC particles according to a Lennard-Jones potential. The expression above is then obtained by integrating the Lennard-Jones potential over the plane and combining some remaining constants such as the interaction strength of the Lennard-Jones and the wall particle density into the effective interaction strength ϵ_mw. In the present work continuous walls are preferred over atomistic walls, i.e., walls made of a lattice of particles, as the implementation of the former is simpler in the case of fluctuating system size.

For the study of how colloidal inclusions disturb the density and the order field of the LC, spheres of radius R_c are introduced in the simulated systems. The interaction energy U_mc between these colloids with the LC particles is given by

$$U_\mathrm{mc}\left(\mathbf{r}, \hat{\mathbf{u}}\right) = \epsilon_\mathrm{mc}\left[a_\mathrm{mc}\left(\frac{\sigma}{r - R_\mathrm{c}}\right)^{10} - b_\mathrm{mc}\frac{1}{r - R_\mathrm{c}}\exp\left(\eta_\mathrm{mc}\left(r - R_\mathrm{c}\right)\right) g\left(\hat{\mathbf{r}}, \hat{\mathbf{u}}\right)\right], \quad (3.30)$$

$$a_\mathrm{mc} = \frac{1 + \eta_\mathrm{mc}\sigma}{9 - \eta_\mathrm{mc}\sigma}, \quad b_\mathrm{mc} = 10\sigma\frac{e^{\eta_\mathrm{mc}\sigma}}{9 - \eta_\mathrm{mc}\sigma}, \quad (3.31)$$

which is almost identical to the model potential in equation (3.16). The interaction strength ϵ_mc and the inverse screening length η_mc have the same meaning as their counterparts in equation (3.16) but they assume different values. Throughout most of the present thesis their values are set to $\epsilon_\mathrm{mc} = 10\epsilon_0$ and $\eta_\mathrm{mc} = 1/2\sigma^{-1}$. In contrast to the potential (3.16) the function Ψ is not used as an anisotropic factor, since the colloids themselves do not have a preferred orientation. Instead, the same anchoring function g is employed as for the interaction (3.29) of the LC particles with the walls. The inter-colloid potential U_cc is given only by the repulsive part of above potential

$$U_\mathrm{cc}\left(r_\mathrm{cc}\right) = \epsilon_\mathrm{cc}\left(\frac{\sigma}{r_\mathrm{cc} - 2R_\mathrm{c}}\right)^{10}, \quad (3.32)$$

where the interaction strength is also chosen to be $\epsilon_\mathrm{cc} = 10\epsilon_0$. An attractive part for the inter colloid interaction is neglected in order to test whether the present LC model in equation (3.16) is able to mediate an effective attraction between different colloids.

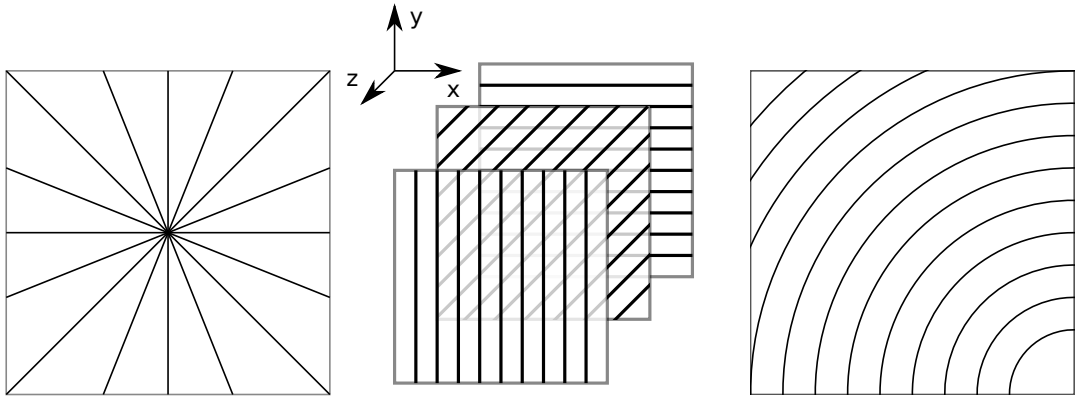

(i) (ii) (iii)

Figure 3.5: Sketches of the basic distortions that director fields can display. (i) shows an example of a director field with a pure splay distortion with a point defect in the center, (ii) shows a pure twist distortion and (iii) shows a pure bend distortion.

3.3 Elastic constants

When considering nematic LCs on the macroscopic scale, the concept of a global director, as defined in section 3.1.1, can be generalized to a director field $\hat{\mathbf{n}}(\mathbf{x})$. This field assigns a unit vector to each point $\mathbf{x}$ within the domain $\Omega \subseteq \mathbb{R}^3$ occupied by the LC fluid. Physically, this unit vector corresponds to the average director of a small region around $\mathbf{x}$. Again it shall be remarked that the sign of the director field holds no physical significance, and that for rigorousness it would be more precise to consider the field of the nematic order tensor $\mathbf{Q}(\mathbf{x})$. In the absence of any external fields, the states of LCs with the smallest potential energy should be those in which the director field is uniform. Any deviation from such a state would increase the system's potential energy. For a director field in three dimensions such deviations can be decomposed into three independent types of distortions as sketched in Figure 3.5: (*i*) splay distortions, where the characteristic curves of the director field are straight but diverging lines, i.e. neighboring curves are not parallel to each other; (*ii*) twist distortions, where, again, the characteristic curves of the director field are confined to planes in which they form straight and parallel lines. The axis, which the curves follow, changes continuously between neighboring layers; (*iii*) in the case of bend distortions, the characteristic curves are truly curved. The free energy associated with the distortions of a director field $\hat{\mathbf{n}}(\mathbf{x})$ is called the distortion free energy (or also Frank free energy) and amounts [28] to

$$F_d = \int \left\{ \frac{1}{2} K_1 \left(\nabla \cdot \hat{\mathbf{n}}\right)^2 + \frac{1}{2} K_2 \left(\hat{\mathbf{n}} \cdot \nabla \times \hat{\mathbf{n}}\right)^2 + \frac{1}{2} K_3 \left(\hat{\mathbf{n}} \times \nabla \times \hat{\mathbf{n}}\right)^2 \right\} \mathrm{d}V, \tag{3.33}$$

where the three elastic coefficients K_1, K_2, K_3 are phenomenological material constants which assign an energy density to splay, twist and bend distortions respec-

tively. Without the interaction of any external fields other than its boundary conditions, the director field of a LC at equilibrium is fully determined by its elastic constants and it can be calculated by just minimization of equation (3.33). In the presence of other external fields, which interact with the LC particles, their director field deforms and deviates from this equilibrium state. In fact, the coupling of external fields to the director field is usually employed in order to determine the elastic constants of a LC, as it is done with electric fields in a Freedericksz' transition [29]. In this thesis, however, another approach as described by Allen and Frenkel [30, 31] is used for determining the elastic constants. This approach makes use of fluctuation relations of the Fourier transform $\hat{\mathbf{Q}}$ of the nematic order tensor field, which is given by

$$\hat{\mathbf{Q}}(\mathbf{k}) = \int \mathbf{Q}(\mathbf{x}) \exp(i\mathbf{k}\cdot\mathbf{x}) \mathrm{d}\mathbf{x} \approx \frac{V}{2N} \sum_{n=1}^{N} \left(3\hat{\mathbf{u}}_n \otimes \hat{\mathbf{u}}_n - \mathbf{1}\right) \exp\left(i\mathbf{k}\cdot\mathbf{x}_n\right). \tag{3.34}$$

In the case that the global director $\hat{\mathbf{n}}$ is aligned along the third axis and the wave vector $\mathbf{k}$ is given by $(k_1, 0, k_3)$ the following relations hold

$$E_{13}\left(k_1^2, k_3^2\right) = \frac{9}{4} \frac{S^2 V k_B T}{\langle \hat{Q}_{13}(\mathbf{k})\, \hat{Q}_{13}(-\mathbf{k}) \rangle} = K_1 k_1^2 + K_3 k_3^2, \tag{3.35}$$

$$E_{23}\left(k_1^2, k_3^2\right) = \frac{9}{4} \frac{S^2 V k_B T}{\langle \hat{Q}_{23}(\mathbf{k})\, \hat{Q}_{23}(-\mathbf{k}) \rangle} = K_2 k_1^2 + K_3 k_3^2, \tag{3.36}$$

where $\hat{Q}_{13}$ and $\hat{Q}_{23}$ are components of the transformed order tensor (3.34) and k_B is Boltzmann's constant.

3.4 Topological defects

Director fields $\hat{\mathbf{n}}(\mathbf{x})$ as sketched previously in section 3.3 are not necessarily continuous in every point $\mathbf{x}$. Sets of points in which the director field is discontinuous, and which cannot be removed by continuously deforming the field, are called defects or disclinations. The latter expression is specifically used for discontinuities of vector fields such as the director field, whereas the former can also refer to discontinuities in more general order fields. In two dimensional bulk systems defects can be point-like (see for example Figure 3.5) and line-like; in three dimensions, they can additionally be sheet-like. Point defects in three dimensions can sometimes also be referred to as hedgehog defects. The study of disclinations is intimately connected to homotopy theory [14]. There are different types of points defects, which can be distinguished by their topological charge. In order to briefly introduce them, we consider a two dimensional system. The director field $\hat{\mathbf{u}}(\mathbf{x})$ in two dimensions maps every point $\mathbf{x}$ from the position space onto a point on the unit circle S^1 on which antipodal points are identified with each other (due to the equivalence of $\hat{\mathbf{u}}$ and $-\hat{\mathbf{u}}$). Now, let a loop in position space be parametrized by a continuous function $c : [0, 1] \to \mathbb{R}^2, t \mapsto \mathbf{x}(t)$.

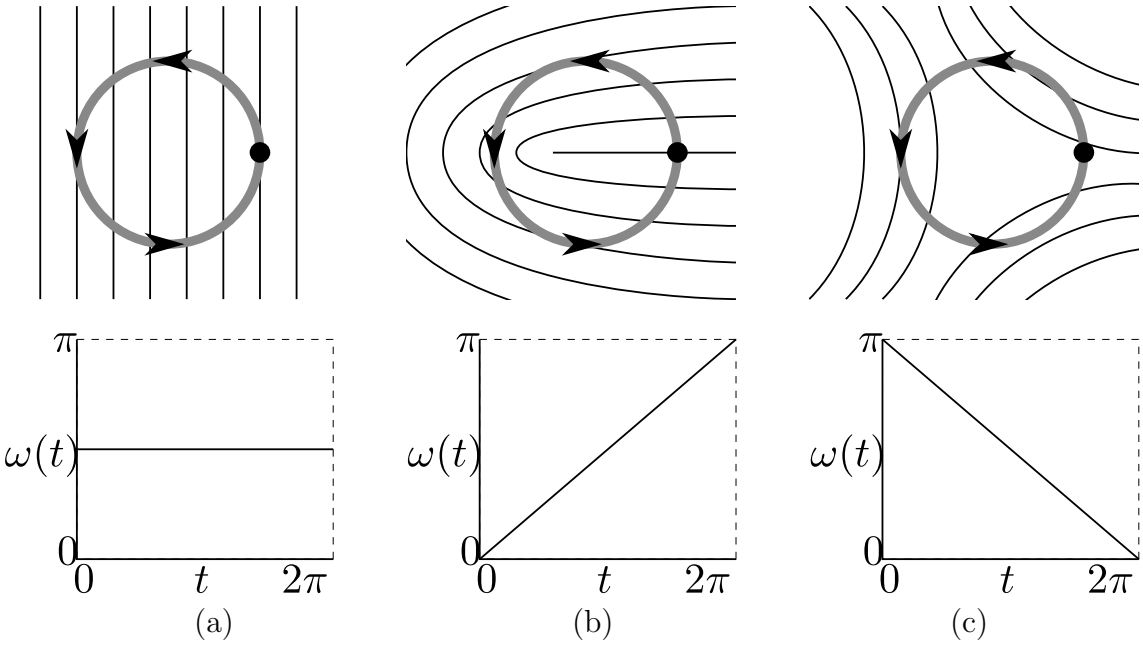

Figure 3.6: Sketch of two dimensional director fields with no defects (a), with a point defect of 1/2 topological charge (b), and with a point defect of $-1/2$ topological charge (c). The bottom row shows the uniform function $\omega_c(t)$.

As long as a loop does not traverse any defects, it defines a continuous function on the unit circle $\omega_c : [0, 1] \to \mathbb{R}$ such that $\hat{\mathbf{u}}(\mathbf{x}(t)) = (\cos(2\pi\omega_c(t)), \sin(2\pi\omega_c(t)))$. Since c is a loop, its start and end point are identical ($\mathbf{x}(0) = \mathbf{x}(1)$) requiring the function ω_c to satisfy the condition $\omega_c(0) = \omega_c(1) + k$, with a half integer number $k \in \mathbb{Z}/2$. The number k is the topological charge of a point defect in two dimensions. It can be shown by more rigorous means [14] that continuous deformation of the loop c or even of the director field itself do not change the topological charge k, as long as the loop c crosses no defects during the deformation. Another consequence following from topological considerations [14] is that the total topological charge within a loop corresponds to the sum of the charges of all topological defects it surrounds. For a director field, which evolves freely in time, this means that the total topological charge is a conserved quantity, as long as the dynamics are continuous. The notion of a charge is not arbitrary. In fact, there are quite a few parallels between defects and elementary particles, besides the conservation of the total charge: topological defects with the same sign in charge repel each other, whereas defects with the opposite sign in charge attract each other [15]. Creation and annihilation of defect pairs of opposite charge is also possible.

Defects cost free energy, as their presence requires distortions of the director field. The number of defects found in the equilibrium state of a director field is therefore as low as the boundary conditions allow. Defects can be stabilized or induced by imposing boundary conditions which are not compatible with a uniform director

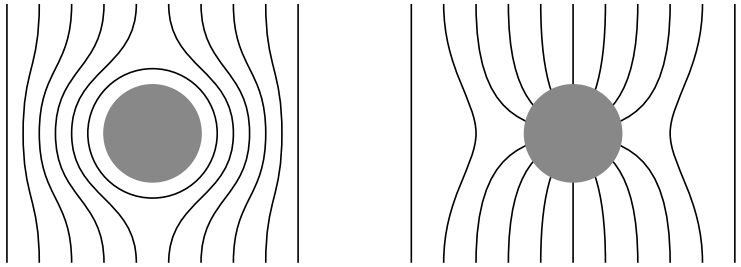

Figure 3.7: Sketches of distortion of the director field and the induced defects close to a circular inclusion with planar anchoring (a) and homeotropic anchoring (b).

field. For example the director field in a circular confinement with homogeneous[2] anchoring needs to contain defects with a combined topological charge of one. Other examples can be given for circular inclusions in the uniform director field (see Figure 3.7). In either case of planar anchoring (director field aligns parallel to surface of the inclusion) or homeotropic anchoring (perpendicular alignment) the director field immediately surrounding the inclusion contains a topological charge of one, while the field far away from the inclusion contains none. This is only possible if in between there exist defects with negative charge to neutralize the positive charge of the inclusion. The type of anchoring influences where the defects are located. In the simplest configuration with planar anchoring one defect of charge -1/2 is found at each pole[3] of the inclusion. The simplest configuration with homeotropic anchoring has the defects at the inclusion's equator. Going from two dimensions up to three dimensions, the circular inclusions become spherical. The corresponding director fields are constructed from the two dimensional configurations by rotating them around the axis of the spherical inclusions. Both point defects next to the sphere with homeotropic anchoring become a single -1/2 disclination loop around the equator. Adequately, this sort of disclination loop is named Saturn ring [32]. In case of the spherical inclusion with planar anchoring, the defects at the inclusions poles remain point-like in nature. This defect structure is commonly known as Boojum defect[4]. Freely moving spherical inclusion, or just colloids in a LC experience interactions which are mediated by the LC and which can for the largest part be understood in terms of minimization of the distortion free energy (3.33). The defects induced by the inclusions, however, play an important role in the details of the interaction between colloids [16].

In smectic A LCs a colloidal inclusion with planar anchoring can lead to the formation of so called focal line defects. These kind of defects consist of discontinuities

[2]The relative angle between director field and boundary is everywhere the same.

[3]Poles and equator of the colloid are refered to with respect of the axis spanned by the director far away from the includion.

[4]A term coined by Mermin who named it after the infamous creature from Lewis Carroll's poe“” *The Hunting of the Snark*”[33–35].

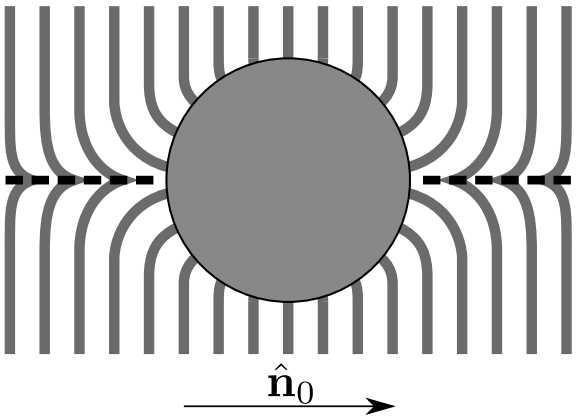

Figure 3.8: Sketch of focal lines caused by a colloidal inclusion with strong planar anchoring in a smectic A phase. The grey lines do not represent the director field but the smectic layers. The focal lines, indicated by the dashes, are the lines in which the normal of the smectic layers changes discontinuously.

of the director field, which arise due to cusp-like deformations of the smectic layers. In order for an inclusion to produce this sort of defects strong surface anchoring is required as well as equidistant inter-layer spacing. Strong anchoring is needed in order to align the LC particles at the colloid's surface with the latter, overcoming the influence of neighbouring particles and deforming the layers of particles. The requirement for constant distances between the layers is fulfilled in ideal smectic A systems, where it leads to the disapearance of twist and bend distortions of the director field. Due to the second condition, the inclusion's perturbation of the layers can propagate through the LC, deforming particle layers which are far away from the inclusion. Due to the planar anchoring conditions, the layers deform in such a way that they form cusps along the axis which goes through the poles of the colloid.

4 Numerical methods

4.1 Equations of motion and integration scheme

For this thesis we use molecular dynamics (MD) simulations in order to study the model LC, i.e., we solve our system's Newton equations of motion by means of a numerical integration scheme. We adapt the integration scheme proposed by Ilnytskyi and Wilson [36], which is designed for the dynamics of rod-like LC particles and already incorporates the equations of motion for a Nosé-Hoover thermostat and Hoover barostat. Throughout this work we are concerned with systems of N particles confined to a box with side lengths L_α, $\alpha = x, y, z$, where each particle n is characterized by a coordinate vector $\mathbf{x}_n$, a velocity $\mathbf{v}_n$ and its mass m_n. Additionally, each LC particle has an orientation, a unit vector $\hat{\mathbf{u}}_n$, associated with it, as well as its time derivative and a moment of inertia I_n. Even though the value of I_n is derived from a prolate ellipsoid, in this model rotations of the particles about their orientation $\hat{\mathbf{u}}_n$ do not contribute to the total energy. It is therefore sufficient to express the moment of inertia as a scalar instead of a tensor. The equations of motion can be derived by means of Hamilton's equations from the Hamiltonian

$$H_0 = \sum_{n=1}^{N} \frac{m_n}{2} \mathbf{v}_n^2 + \sum_{n=1}^{N} \frac{I_n}{2} \mathbf{w}_n^2 + \sum_{n=1}^{N-1} \sum_{l>n}^{N} U_{\mathrm{mm}} \left(\mathbf{x}_n - \mathbf{x}_l, \hat{\mathbf{u}}_n, \hat{\mathbf{u}}_l, \right) - \sum_{n=1}^{N} \lambda_n c \left(\hat{\mathbf{u}}_n \right), \quad (4.1)$$

where the coefficients λ_i are Lagrange multipliers which, together with the constraint $c(\hat{\mathbf{u}}) \equiv \hat{\mathbf{u}}^2 - 1$, limit the orientation vectors $\hat{\mathbf{u}}_n$ to the unit sphere. As the Hamiltonian is not explicitly time dependent, the total energy E of the system is conserved. Assuming ergodicity of the system, simulations are only able to sample the microcanonical (NVE) ensemble of the system, i.e. the collection of all possible configurations sharing the same number of particles N, volume V and total energy E. As a consequence, the system's temperature T as defined via the kinetic energy is subject to fluctuations as is the pressure P. In order to make the simulations'

results more comparable to real world systems we are interested in performing simulations in the canonical (NVT) ensemble, in which the temperature T is fixed and the energy E fluctuates, or to simulate in the isothermal-isobaric (NPT) ensemble, in which additionally the pressure P is constant and the volume V is allowed to vary. The most common way to achieve this is by adding a Nosé-Hoover thermostat [36–38] and a Hoover barostat [36, 38, 39] to the system. The basic premise of these methods is to expand the original system by additional degrees of freedom. By choosing an appropriate coupling between the original system and the additional coordinates, the projection of the trajectories of the extended system onto the original one follows the Maxwell-Boltzmann distribution. In the following, η will denote the coordinate of the thermostat, ξ denotes its generalized momentum and Q refers to its mass. The barostat's coordinate V is incidentally the system's volume, ξ_P and Q_P denote its generalized momentum and mass, respectively. Following Ilnytskyi and Wilson [36] the equations of motion for the extended system are given by

$$\dot{\mathbf{x}}_n = V^{-1/3}\mathbf{v}_n, \qquad \dot{\mathbf{v}}_n = \mathbf{f}_n - (\xi + \xi_p)\,\mathbf{v}_n, \tag{4.2}$$

$$\dot{\mathbf{u}}_n = \mathbf{w}_n, \qquad \dot{\mathbf{w}}_n = \mathbf{g}_n^{\perp} - \xi\mathbf{w}_n - \lambda\mathbf{u}_n, \tag{4.3}$$

$$\dot{\eta} = \xi, \qquad \dot{\xi} = Q^{-1}\left(fT - fT_0\right), \tag{4.4}$$

$$\dot{V} = 3V\xi_p, \qquad \dot{\xi}_p = 3VQ_p^{-1}\left(P - P_0\right), \tag{4.5}$$

where the reduce force $\mathbf{f}_n$ is defined as $\mathbf{f}_n \equiv\ m_n^{-1}(\partial\, U_\mathrm{mm}/\partial\mathbf{x}_n)$ and $\mathbf{g}^{\perp}$ is the component of $\mathbf{g}_n \equiv\ I_n^{-1}(\partial\, U_\mathrm{mm}/\partial\hat{\mathbf{u}}_n)$ which is perpendicular to the orientation $\hat{\mathbf{u}}_n$. The expression f refers to the total number of degrees of freedom. In case of N LC particles with three translational and two rotational degrees of freedom, f amounts to $f = 5N$. The instantaneous temperature T and pressure P are given by

$$T = \frac{1}{f}\left(\sum_{n=1}^{N} m_n\mathbf{v}_n^2 + \sum_{n=1}^{N} I_n\mathbf{w}_n^2\right), \tag{4.6}$$

$$P = \frac{1}{3V}\left(\sum_{n=1}^{N} m_n\mathbf{v}_n^2 + \mathbf{x}_n\cdot\mathbf{F}_n\right). \tag{4.7}$$

Since these are the equations of motion of a Hamiltonian system, the stability and accuracy of the simulations can be improved by integrating them with a scheme which preserves the system's symplectic flow [40]. The velocity-Verlet (VV) algorithm [41] is a simple integration scheme belonging to a family of symplectic integrators [41, 42] and is computationally not much more expensive than the Euler method. For a simple set of equations $(\dot{\mathbf{x}}, \dot{\mathbf{v}}) = (\mathbf{v}, \mathbf{f}(\mathbf{x}))$ the integration scheme can be written in three steps

$$\begin{aligned}
&(i) \qquad \mathbf{v}\left(t + \Delta t/2\right) = \mathbf{v}\left(t\right) + \frac{1}{2}\mathbf{f}\left(\mathbf{x}\left(t\right)\right)\Delta t,\\
&(ii) \qquad \mathbf{x}\left(t + \Delta t\right) = \mathbf{x}\left(t\right) + \mathbf{v}\left(t + \Delta t/2\right)\Delta t,\\
&(iii) \qquad \mathbf{v}\left(t + \Delta t\right) = \mathbf{v}\left(t + \Delta t/2\right) + \frac{1}{2}\mathbf{f}\left(x\left(t + \Delta\ t\right)\right).
\end{aligned} \tag{4.8}$$

In [36] the authors present how to adapt the VV algorithm to the above equations of motion (equations (4.2-4.5)), which we implement and use for this thesis. However, due to the thermostat and barostat, which dynamically scales the particles coordinates, the resulting integration steps are more involved.

4.2 Periodic boundary conditions

For the most part we are concerned with studying bulk properties of the model LC. To this end it is advantageous to use periodic boundary conditions, since by doing so small systems can be simulated without having to deal with boundary effects, while requirering low additional computational cost. Periodic boundary conditions only need to be considered for the calculation of distances between two points and after calculating the new particle positions $\mathbf{x}_n$. In the latter case, it has to be checked for each particle n whether any component x_n^i of its new position lies ouside the simulation box' margins. If that is the case for any of the x_n^i, they are reinserted into the box by shifting them by the corresponding side length L^i of the box. For the distance calculations, it needs to be considered, that each point is equivalent to its periodic image ($x^i \sim x^i + kL^i$), $k \in \mathbb{N}$. Therefore, it makes sense to define the distance between two points $\mathbf{x}_n$ and $\mathbf{x}_l$ as the Euclidean norm of the shortest vector $\mathbf{r}_{nl}$ pointing from $\mathbf{x}_n$ to $\mathbf{x}_l$ or any of its periodic images. By choosing a Cartesian coordinate sytem, such that the axes are aligned with the simulation box' sides, the origin coincides with center of the box, then the components of the vector $\mathbf{r}_{nl}$ are explicitely given by

$$r_{nl}^i = \left(x_n^i - x_l^i\right) - \left\lfloor \frac{x_n^i - x_l^i}{L^i} \right\rceil L^i, \tag{4.9}$$

where $\lfloor \cdot \rceil$ denotes rounding to the argument's closest integer. For some systems, the periodic boundary conditions are eliminated along one axis, by introducing walls perpendicular to it and the above considerations need to be applied only along the remaining axes.

4.3 Neighbor list

For the sake of computation convenience, interactions between particle pairs are neglected when they are separated by a distance $d > d_\mathrm{c}$ where $d_\mathrm{c} = 3\sigma$ is the cutoff distance. We make use of a linked-list cell [43] in order to avoid checking all $N(N-1)/2$ inter-particle distances before every force calculation, and therefore saving even more computational time. This method divides the simulation box into equally sized, rectangular cells of volume V_c and side lengths l_i. Before each integration cycle a linked-list is generated for all cells, listing the particles they contain. When calculating the forces acting on a particle n only the distances which lie within the same cell as n or within adjacent cells are evaluated. For all particles

in one cell this amounts on average to $V_c\rho(\nu V_c\rho - 1)$ distance checks, where $\rho = N/V$ denotes the particle density and $\nu = \nu' + 1$, with ν' denoting the number of adjacent cells. Taken over the whole simulation box those are $N(\nu\ V_c\rho - 1)$ distance checks. Considering that the initialization of the linked list also takes N computation steps, the total computation cost scales much better with the system size ($\mathcal{O}(N)$) compared to the brute force method of evaluating all pairs ($\mathcal{O}(N^2)$). The cell's side lengths l_i should not be smaller than the cutoff d_c, otherwise particle pairs, lying within the cutoff distance, might be ignored when calculating interactions. Choosing larger side lengths l_i slows the simulations down, as more distances between non-interacting pairs of particles are checked.

There is a caveat when parallelizing the generation of the linked-lists. This has to be taken into account as we parallelize our simulations using CUDA. In the present implementation one parallel process is started for every particle n, in which the particle's cell is determined and the particle's index is written into the list. The order in which the particles are listed depends on the order in which the processes finish, which is variable, thereby introducing randomness into the simulation. Due to the non-associativity of the numerical addition of floating-point numbers [44] this randomness can propagate through the calculation of the forces, velocities and positions of the particles, affecting the exact reproducibility of simulations. Two possibilities of getting rid of this non-reproducibility are to either serialize the linked-list generation or to sort the lists after their generation, both of which are slower than just generating the lists in parallel. Since this extra stochastic noise does not change the resulting configurations qualitatively nor does it change averaged quantities, we accepted the noise in exchange for sligthly faster performance.

4.4 Choice of units and constants

We list below the numerical values of the model's parameters, which were used throughout the simulations. We choose the scales of physical quantities such that lengths are given in units of σ and energies are given in units of ϵ_0 (see equation 3.16 for reference). Masses will be given in units of LC particles' mass denoted by μ. The temperature scale θ is chosen such that Boltzmann's constant k_B is unity. All other quantities can be expressed in terms of the above quantities. The time step of the numeric integration amounts to $\Delta t = 0.001\ \sigma\sqrt{(\mu/\epsilon_0)}$.

In order to set the value of the LC particle's moments of inertia I, we approximated the particles with prolate ellipsoids with homogeneously distributed mass and with semi-major and semi-minor axes a_l and a_s. The values of the semi-axes have been determined from radial distribution functions of results obtained from Monte Carlo (MC) simulations prior to performing the simulations in this thesis. As it turns out using this model results in a moment of inertia which is only slightly smaller than that of one dimensional unit rod with homogeneously distributed unit mass ($I_{\mathrm{Rod}} = 1/3$).

Table 4.1: Numerical values of the model's parameters.

ϵ_1	$4\epsilon_0$
ϵ_2	$-8\epsilon_0$
η	$3\sigma^{-1}$
a_l	0.8876σ
a_s	0.3675σ
I	$0.3151\mu\sigma^2$

5 Results

5.1 Preliminary parameter exploration

In a preliminary study of the model proposed by Hess and Su (see section 3.2.1), systems with different parameter pairs ϵ_1 and ϵ_2 are explored numerically, in order to probe for parameter pairs which result in smectic A phases. For this purpose, we limit the parameter set of interest to the triangular subset in ϵ_1-ϵ_2-space, as defined in section 3.2.3, from which several parameter pairs are chosen (see Figure 5.1) for numerical investigation. For each parameter pair a series of systems is simulated, each system consisting $N = 4000$ particles confined to cuboid simulation boxes with periodic boundary conditions. The simulations are performed in the NPT ensemble by means of a Hoover barostat and Nosé-Hoover thermostat. For most parameter pairs ϵ_1, ϵ_2 we choose pressure values $P \in [0.6, 1.0]$ in steps of $\Delta P = 0.1$. The temperature range and step size is adjusted manually, according to the simulation result, but generally temperature values lie in the range of $T \in [0.1, 2.0]$, the step size being either $\Delta T = 0.1$ or $\Delta T = 0.2$. For some systems additional simulations are conducted for temperature ranges in which a transition from nematic to crystalline systems is observed, in order to enhance the temperature resolution. The simulated systems are initialized from randomly generated isotropic configurations and equilibrated for at least 25×10^4 iteration steps. For some systems this simulation length seems insufficient for reaching equilibrium, in which case the simulations are extended to a total amount of 5×10^5 iteration steps. To evaluate the equilibration of the systems, the evolution of macroscopic properties of the systems, such as total potential energy, kinetic energy, volume, etc., are evaluated.

An initial analysis of the simulation results can be made by calculating the nematic order parameter S and the smectic A order parameter Λ for the final configurations. Configurations are classified as nematic if $S > 1/3$ and smectic A if additionally $\Lambda > 1/3$, the latter condition being somewhat arbitrary. According to these conditions we are able to find nematic and smectic A phases, sometimes also isotropic phases.

However, closer visual inspection of the apparent smectic systems reveals that they look more like proper crystals as the particles within the layers are arranged in a very regular fashion. The radial distribution functions of these systems provide further evidence for this; they are more similar to a radial distribution of a crystal, as they show spikes, even at larger distances r, and sometimes they do not approach unity at large distances r.

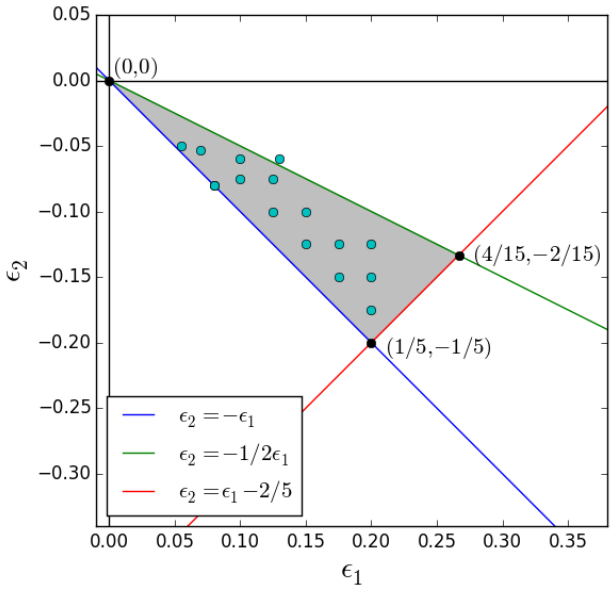

Figure 5.1: Chart of all parameter pairs (ϵ_1, ϵ_2) given by the light blue circles for which simulations were performed. Parameter pairs within the shaded, triangular region produce the energetic hierarchy, which is assumed to allow the formation of smectic phases (see section 3.2.3).

It should be noted, that the parameter pair $2\epsilon_1 = -\epsilon_2 = 0.8$ can result in smectic A phases, when using the modified model potential in equation (3.16), even though it lies outside the parameter set (as defined in section 3.2.3) which was assumed to be necessary for the formation of such phases. In fact, this parameter pair yields the energy hierarchy $U_{\mathrm{ss}} < U_{\mathrm{X}} < U_{\mathrm{T}} < U_{\mathrm{ee}}$ as opposed to the initially assumed hierarchy $U_{\mathrm{ss}} < U_{\mathrm{X}} < U_{\mathrm{ee}} < U_{\mathrm{T}}$, proving the initial assumption to be incorrect. But more importantly, this parameter pair results in a purely repulsive pair potential for particles in the end-to-end configuration as can be seen in Figure 3.3. Using the potential proposed by Hess and Su (3.12) for simulations with this pair of parameters ϵ_1 and ϵ_2 results in systems in which the particles arrange in sheets, which appear to repel each other, as they bend and curl up in a very wild fashion.

One possible reason for the difference in behaviour between this potential and the modified potential in equation (3.16) may be the different decay behaviour of the potentials in the repulsive end-to-end configuration. At large distances r, the

former potential decays like r^{-6} whereas the leading term of the latter potential being proportional to r^{-10}, thus decaying much faster. Also the attractive well seems to be sharper than for tha modified potential. Another possible reason for the inability of the potential by Hess and Su, to form stable smectic layers, may be due its particles' small aspect ratio (compare with Figure 3.3). In the following we will consider only the modified Hess-Su potential in equation (3.16), as this produces appropiate smectic phases.

5.2 Phase diagram

We study the influence of pressure and temperature on the model given by equation (3.16) by generating a phase diagram (see Figure 5.2). To that end we simulate systems of N=6000 particles confined to a cuboid simulation box with periodic boundary conditions. The simulations are run in the NPT ensemble by means of a Nosé-Hoover thermostat and a Hoover barostat [38]. Different systems are simulated for different values of pressure P and temperature T. Simulations at the highest temperature were initialized with randomly generated configurations in which the particles' positions $\mathbf{x}_i$ are distributed uniformly in the simulation box and the orientations $\mathbf{u}_i$ are distributed uniformly on the unit sphere. At lower temperatures the simulations are initialized with the equilibrated, final configuration of the simulation with the next higher temperature T and the same pressure P. This way of initialization saves computation time when equilibrating the systems, as it ensures that the starting configuration is already close to an equilibrium configuration, resulting overall in a cleaner and faster equilibration process. Within the chosen pressure and temperature range and using the initialization method described above, 2×10^5 integration steps are deemed sufficient in order for the systems to reach equilibrium. The nematic and smectic order parameters S and Λ of the equilibrated systems are calculated following equations (3.1) and (3.11). Systems with a nematic order parameter of $S > 1/3$ are classified as nematic, otherwise they are considered to be isotropic. Nematic systems with a smectic order parameter of $\Lambda > 1/3$ are classified as smectic A.

The phase diagram resulting from the simulations is shown in Figure 5.2. It shows that the studied model (equation (3.16)) produces isotropic, nematic and smectic A phases. The formation of different phases is primarily dependent on temperature, with smectic A phases forming at low temperatures (below $T \approx 0.78$), nematic phases forming at intermediate temperatures (up to $T \approx 0.84 - 0.86$) and isotropic phases forming at high temperatures. Increasing the pressure widens the temperature range in which the nematic phase is stable.

A detailed study of the temperature dependence of the nematic and the smectic order parameters S and Λ is shown in Figure 5.3 for pressure $P = 1.0$ From this graph it can be seen, that the isotropic nematic (IN) transition occurs between $T = 0.84$ and $T = 0.86$. Further inspection of Monte Carlo simulations of the same model system [45] locates the transition at a slightly higher temperature $T_{\mathrm{IN}} \approx 0.87$.

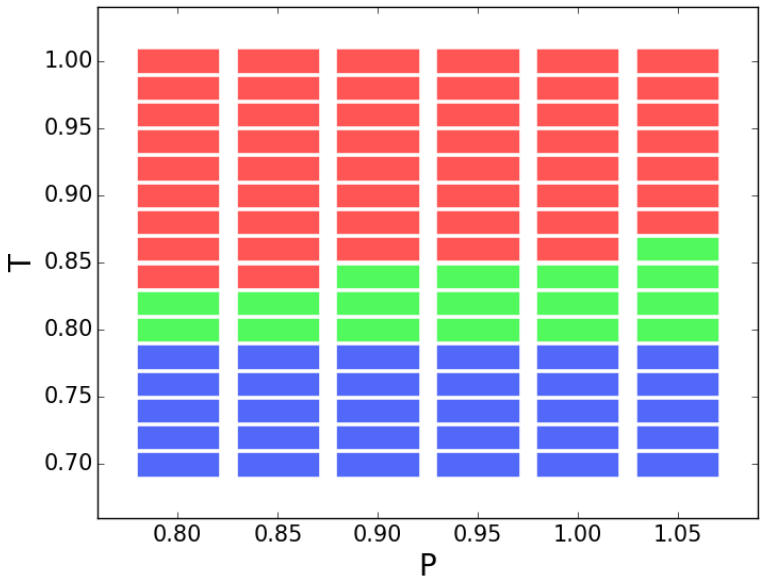

Figure 5.2: Phase diagram of the model LC. Blue rectangles represent simulations in which the final configuration is classified as smectic A. Green rectangles represent simulations in which the final state is classified as nematic. Red rectangles represent simulations with an isotropic final state.

For temperatures larger than T_{IN} the system appears to be isotropic, even though the nematic and smectic order parameter S and Λ do not entirely vanish. The parameters S and Λ fluctuate about values of $S = 0.014$ and $\Lambda = 0.023$. The non-vanishing of the order parameters is attributed to the finite size of the simulated system; they are expected to become smaller with increasing system size. As the temperature drops below $T = 0.6$ the nematic order parameter S sharply increases to values larger than $S = 0.6$. It steadily grows larger as the temperature decreases further, even when the system becomes smectic A. The rate at which S grows becomes increasingly smaller, though.

Down to temperatures of $T \approx 0.8$ the smectic order parameter Λ remains relatively small as it does not exceed values of $\Lambda = 0.1$. In case of the simulation series with pressure $P = 1.0$ the smectic order parameter Λ seems to be significantly larger than its value in the isotropic phase ($\Lambda \approx 0.03$). In comparison to the simulation runs at other pressures and with Monte Carlo simulations [45], however, it appears as if at temperatures just below T_{IN} the order parameter Λ should not change much from its value in the isotropic phase, and that the simulation series at pressure $P = 1.0$ is somewhat of an outlier. For lower temperatures Λ increases quite strong at first and then levels off again.

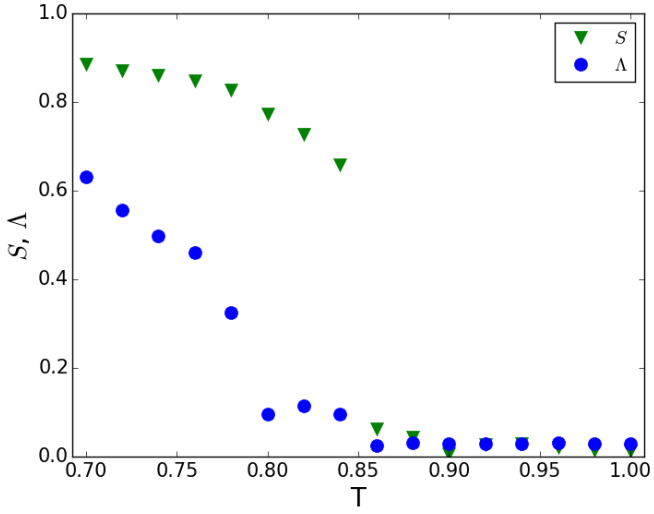

Figure 5.3: Temperature dependence of the nematic order parameter S and the smectic A order parameter Λ at pressure $P = 1.0$.

5.3 Elastic constants

Several series of simulations are performed in order to estimate the splay, twist and bend elastic constants K_1, K_2, K_3, respectively, and to inspect their temperature dependence. The elastic constants are obtained by probing the functions $E_{13}(\mathbf{k})$ and $E_{23}(\mathbf{k})$ (as defined in equations (3.35) and (3.36)). Both functions are probed along wave-vectors $\mathbf{k} = (k_1, 0, 0)$ and $\mathbf{k} = (0, 0, k_3)$, where the smallest values of the wave-numbers k_1 and k_3 are inversely related to the simulation box' length and height. All simulations are performed in the NVT ensemble in order to avoid fluctuations of the size of the simulation box and consequently, uncertainties of the wave numbers. For various temperatures T in the nematic phase two series of simulations are carried out: one in which systems of varying lengths are simulated and another one in which the simulated systems differ in height, thus varying the wave numbers k_1 or k_3. When varied, the simulation box' length (height) takes on values between $L = 10\sigma$ and $L = 20\sigma$, the remaining dimensions are always kept at 10σ. The smallest wave numbers, which are considered in each simulation, are given by $2\pi/L$, where L corresponds to either the simulation box' length or height. For each system the number of LC particles is chosen such that the particle density ρ is as close as possible to the equilibrium particle density, calculated with the simulations of the phase diagram (see section 5.2) at pressure $P = 1.0$ and the corresponding temperature T. Before the equilibration process, the LC particles are distributed randomly within the simulation box but their orientations $\hat{\mathbf{u}}_n$ are all aligned along the third axis. The systems are equilibrated for at least 2×10^5 integration steps; at temperatures lower than $T = 0.80$, the equilibration is extended to 3×10^5 integration steps. Afterwards, the systems are left to evolve freely for 10^6 iteration steps during

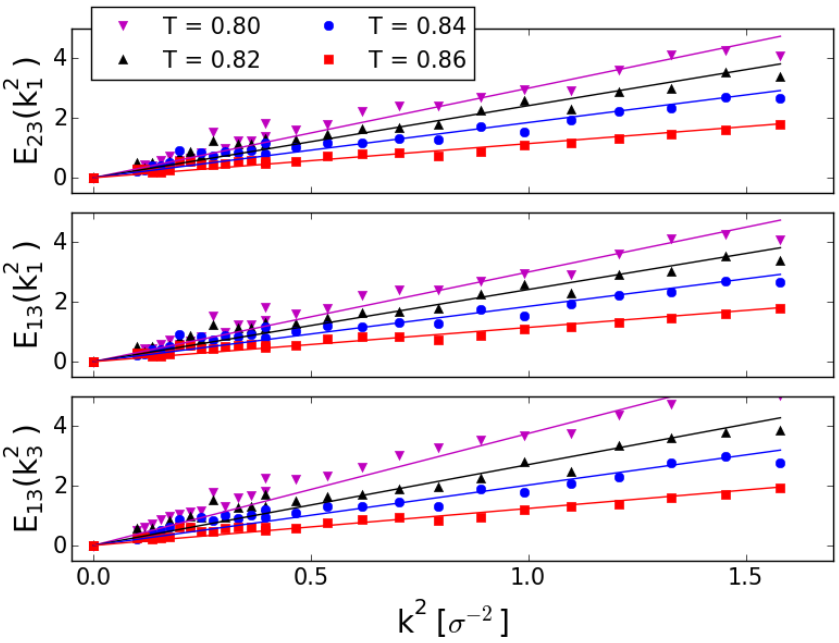

Figure 5.4: Results for the quantities E_{13} and E_{23} along the direction $(1, 0, 0)$, and also for the quantity E_{13} along the direction $(0, 0, 1)$. Lines show linear regressions on the corresponding data.

which the Fourier transforms of the order tensor $\hat{\mathbf{Q}}$ are calculated every 50 iteration steps. The results for E_{13} and E_{23} are shown in Figure 5.4. Eventually, making use of relations (3.35-3.36), the elastic constants are obtained by performing linear regressions on the data in Figure 5.4. The elastic constants and their temperature dependence are shown in Figure 5.5.

As can be seen, all three elastic constants increase with decreasing temperature. At high temperatures (roughly $T > 0.84$) all three constants take on almost the same values. For lower temperatures the three constants start to differ from each other. The bend and twist elastic constants K_2 and K_3 grow much stronger than the splay elastic constant K_1 as the systems approach the smectic A phase with decreasing temperature. This seems to be consistent with theory [1], which states that twist deformations are not present in smectic A phases whereby the twist elastic constant K_2 should diverge in this phase in order for the corresponding deformations to be energetically unfavorable. It is interesting, that the behavior of these results is qualitatively comparable to experimental measurements of octylcyanobiphenyl (8CB) [9].

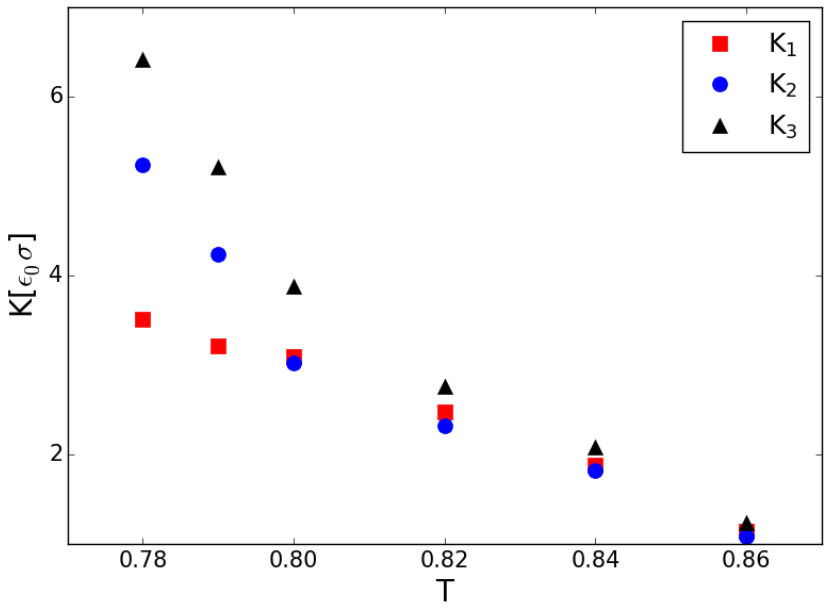

Figure 5.5: Temperature dependence of the splay (K_1), twist (K_2) and bend (K_3) elastic constants.

5.4 Diffusion

We study the self-diffusion of the present model in the bulk phase. In order to do so, we run simulations with $N = 4 \times 10^3$ LC particles contained in a cuboid confinement with periodic boundary conditions. All simulations are run in the NPT ensemble, leaving the pressure fixed at $P = 1.0$. Simulations are run for temperatures $T \in [0.70, 1.00]$ in steps of $\Delta T = 0.02$. The initial configurations are generated with sequential equilibration, just like the simulations of the phase diagram (see Section 5.2). For each simulation the equilibration was done for at least 2×10^5 integration steps. For some simulations at lower temperatures (e.g. at $T = 0.70$) the equilibration needs to be extended up to a total of 6×10^5 integration steps in order for the energies to settle, only fluctuating about stationary values. Afterwards, the equilibrated systems are run for 10^6 integration steps, while snapshots of the particles positions $\mathbf{x}_i$, orientations $\mathbf{u}_i$ and the system size are taken according to a half logarithmic, half linear time-scale: initially the time-intervals between two successive snapshots are doubled, i.e. snapshots are taken after the first integration step then after the second, the fourth, and so on. Every 2^{16} integration steps, the interval doubling is reset, i.e. snapshots are taken after 2^{16} and one steps, after 2^{16} and two steps and so on. This way of taking snapshots allows us to observe the systems' dynamics on different time-scales with just a moderate need of disk space and computation time for writing out the configurations. Using these sets of configurations, the mean square displacement (MSD) and the component-wise MSD

of the particles can be computed according to

$$\langle \Delta r^2_{\parallel,\perp} \rangle (\Delta t) = \frac{1}{N} \sum_{n=1}^{N} \Delta \mathbf{x}^2_{n\parallel\perp} (\Delta t) \tag{5.1}$$

with

$$\Delta \mathbf{x}_{n\parallel\perp} (\Delta t) = \sum_{\alpha=1}^{A} \Delta \mathbf{x}_{n\parallel,\perp} (\Delta t_\alpha), \quad \text{with } \Delta t = t_A - t_0 \tag{5.2}$$

$$\Delta \mathbf{x}_n (\Delta t_\alpha) = \mathbf{x}_n (t_\alpha) - \mathbf{x}_n (t_{\alpha-1}) \tag{5.3}$$

$$\Delta \mathbf{x}_{n\parallel} (\Delta t_\alpha) = (\Delta \mathbf{x}_n (\Delta t_\alpha) \cdot \hat{\mathbf{u}}_n (t_\alpha)) \hat{\mathbf{u}}_n (t_\alpha) \tag{5.4}$$

$$\Delta \mathbf{x}_{n\perp} (\Delta t_\alpha) = \Delta \mathbf{x}_n (\Delta t_\alpha) - \Delta \mathbf{x}_{n\parallel} (\Delta t_\alpha) \tag{5.5}$$

Physically, $\langle \Delta r^2_{\parallel} \rangle$ represents the MSD in the direction of the molecules orientation, and $\langle \Delta r^2_{\parallel} \rangle$ in the orthogonal direction. Results for these quantities in the smectic A, nematic and isotropic phase can be seen in Figure 5.6. In the double logarithmic representation, all MSDs fall on the same curve with slope two at observation times smaller than $\Delta t = 10^0$, irrespective of the temperature, the nematic or the smectic order, showing that all particles move ballistically within this time scale. At observation times of about $\Delta t = 10^{-1}$ the systems reach a transient regime; the MSD-curves of the different phases fan out from each other and their slopes start to decrease. From observation times $\Delta t = 2$ on, the MSD-curves of the isotropic and the nematic systems have a slope of one, indicating diffusive movement of the particles. However, in the case of the smectic A systems, the MSD along the particles' orientations enters a subdiffusive regime, visible in the corresponding curve as a region in which the slope of the MSD lies below one. But also for these systems the MSD along the particles axes becomes diffusive for observation times $\Delta\, t > 1.5 \times 10^2$. The subdiffusive regime for the motion along the LC particles' axes is indicative of the one-dimensional order along the director in the smectic A phase. Once the LC particles are aligned in layers, the repulsion between particles in the end-to-end configuration inhibits the movement of particles between neighboring layers. Eventually, the movement of the particles within a layer will open a gaps, allowing inter-layer movement and diffusion of particles between layers. On the other hand, the absence of a subdiffusive regime for the particles' movement perpendicular to their axes shows that the particles indeed behave like a liquid within the smectic layers, as is expected of this kind of phase.

Parting from the MSDs, the diffusion coefficients $D_\parallel$, $D_\perp$ along their corresponding directions, can be defined via the Einstein relations

$$D_\parallel = \lim_{t\to\infty} \frac{\langle \Delta r^2_{\parallel} \rangle (t)}{2t}, \tag{5.6}$$

$$D_\perp = \lim_{t\to\infty} \frac{\langle \Delta r^2_{\perp} \rangle (t)}{4t}, \tag{5.7}$$

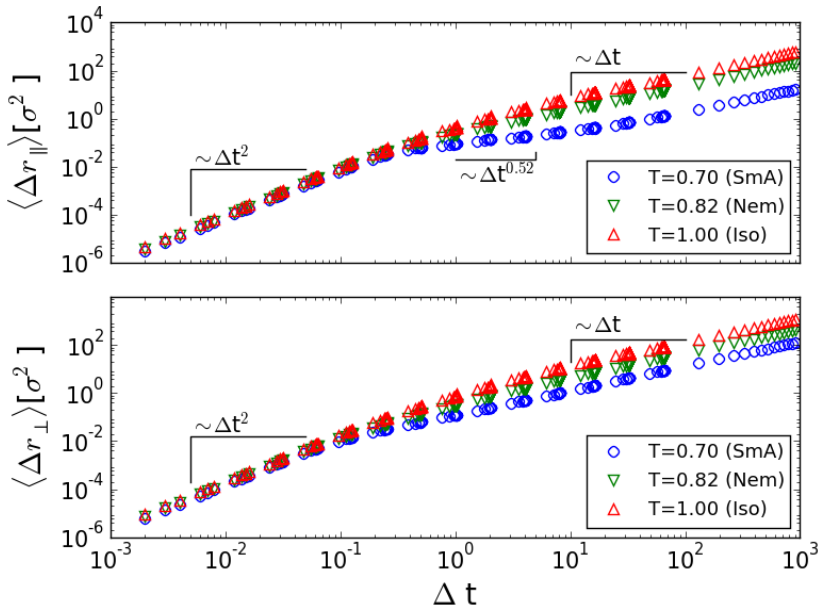

Figure 5.6: Component-wise MSD of the molecules at different temperatures T at pressure $P = 1.0$. At temperature $T = 0.70$ the system is nematic A, at $T = 0.82$ the system is nematic and at $T = 1.00$ the system is isotropic.

where the denominators differ by a factor of two, since the displacement $\Delta r_{\parallel}$ takes place in one dimension whereas $\Delta r_{\perp}$ takes place in two. Taking the number of dimensions into account, in which the motion happens, results in the diffusion coefficient being independent of it. Using this definition, the values of the diffusion coefficients can be estimated by fitting a linear function on the diffusive regime of the MSD data, which follow a slope of one. The resulting values for $D_{\parallel}$ and $D_{\perp}$ are shown in Figure 5.7. The same has been done for systems at pressures $P \in [0.8, 1.0]$ with $\Delta P = 0.5$ and with coarser temperature resolution, the results are shown in Figure 5.8.

From Figure 5.7 we see that the diffusion coefficients are monotonically increasing functions of the temperature T. The three different phases, the smectic A phase, the nematic phase and the isotropic phase can be clearly distinguished by the behaviour of these functions. Passing from the isotropic phase into the nematic phase, there is a sharp drop in both diffusion coefficients $D_{\parallel}(T)$, $D_{\perp}$ and their slopes becom much steeper. At the nematic-smectic A transition, there is no jump in the diffusion coefficients but there is a sharp change in the slopes of $D(T)_{\parallel}$ and $D(T)_{\perp}$, the slope being less steep in the smectic A phase than in the nematic phase. At high temperatures in the isotropic phase, both diffusion coefficients $D_{\parallel}$ and $D_{\perp}$ are practically indistinguishable from each other. This is expected as this phase lacks a distinguished spatial direction. As the system enters the nematic phase, diffusion becomes slightly anisotropic, with $D_{\parallel} > D_{\perp}$. This feature has also been found experimentally [46], and could be understood as trading orientational entropy, thereby

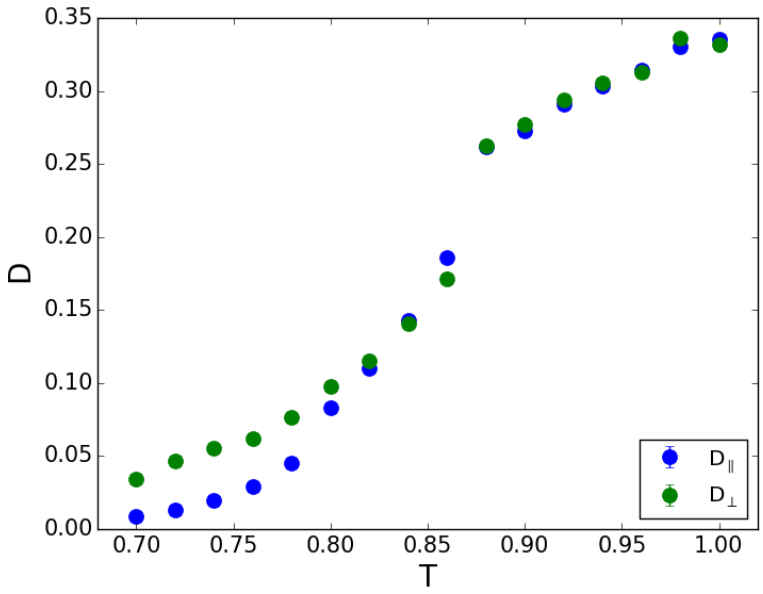

Figure 5.7: Temperature dependence of the diffusion coefficients at pressure $P = 1.0$.

reducing it, in favor of increased translational entropy. For lower temperatures in the nematic phase ($T \approx 0.82$) the anisotropy of the diffusion coefficients is inverted as $D_\perp < D_\parallel$. As the system becomes smectic A, the anisotropy of both diffusion coefficients becomes much more pronounced. The anisotropy of the diffusion coefficients in the smectic A phase stems from the transient subdiffusive movement along the director and thus also reflects the layered structure.

The comparison between systems at different pressures (see Figure 5.8) basically shows the same behaviour of the diffusion coefficients. It also shows that the diffusion coefficients for pressures below $P = 0.95$ rapidly increase between temperatures $T = 0.80$ and $T = 0.85$, indicating the transition from nematic to isotropic. For the pressures $P = 0.95$ and $P = 1.0$ the transition seems to occur at a temperature between $T = 0.85$ and $T = 0.90$, showing that the temperature range of the nematic phase increases with increasing pressure, as was observed in the phase diagram (Figure 5.2). Also, the diffusion coefficients slighlty decrease with increasing pressure.

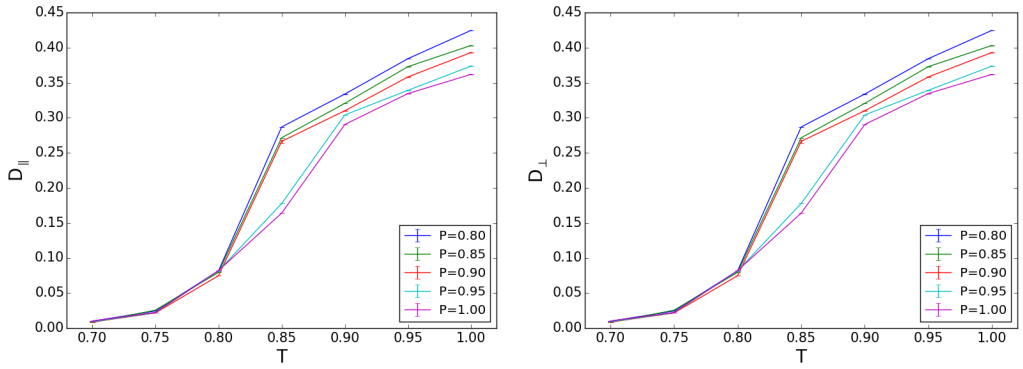

(a) (b)

Figure 5.8: Temperature dependence at different pressures P for the diffusion coefficients $D_{\parallel}$ along the director (a) and the diffusion coefficients $D_{\perp}$ perpendicular to the director (b).

5.5 Colloid-induced defects

We study the steady state of the model in the presence of a colloidal inclusion, both, in the nematic and in the smectic A phase. Due to the microscopic nature of MD simulations, it is necessary to undertake some coarse graining in order to estimate the simulated systems' local nematic order S and the local particle density ρ. To that end, a three dimensional grid is superimposed on the simulated systems, by dividing their volumes in to small bins. For each bin the nematic order tensor Q is calculated according to equation (3.1) using only the particles contained in that bin. Also, the number of particles in each bin is recorded in order to estimate the particle density ρ.

The systems simulated here contain $N = 2 \times 10^4$ freely moving LC particles as well as a colloid which is fixed to the origin of the simulation box. Throughout these simulations, the radius of the colloid is set to $R_C = 3\sigma$. Simulations are performed for homeotropic anchoring between colloid and LC particles, as well as planar anchoring. The simulations are performed in the NPT ensemble within a cuboid simulation box with periodic boundary conditions. Simulations are done for temperatures $T \in [0.70, 1.0]$ in steps of $\Delta T = 0.02$ in order to simulate smectic A, nematic and isotropic phases. For all simulations the pressure is set to $P = 1.0$. The initial configurations are generated randomly according to uniform distributions of the positions and the orientations. They are then equilibrated for 2×10^5 iteration steps. Afterwards, the system is left to evolve freely over the course of 10^6 integration steps. For each bin, the average nematic order tensor Q, as well as the number of particles it contains, is updated every 50 integration steps.

5.5.1 Homeotropic anchoring

For an interaction strength of $\epsilon_{\mathrm{mc}} = 1\epsilon_0$ and an inverse screening length of $\eta = 0.5\sigma^{-1}$, the nematic systems exhibit disclinations loops, or Saturn rings, as is expected and which is comparable to previous experimental [21, 32] and numerical [47**?** , 48] results. These disclination loops are visible as annular regions, centered around the colloid in the y-z planes, in which the nematic order drops below $S = 1/3$. In the cross sections through the x-y plane (see Figure 5.9) the disclination rings are cut forming two diffuse regions of reduced nematic order. The director fields in the centers of these regions clearly show -1/2 point defects. The director fields directly surrounding the colloids (up to roughly $\Delta\ r \approx 2\sigma$ from their surface) are oriented perpendicular to its surface. Within these shells, the nematic order is higher than in regions further away from the colloid (e.g., in case of $T = 0.84$ the average nematic order far away, $r > 5\sigma$, from the colloid is about $S \approx 0.6$, whereas the nematic order close to the colloid is about $S \approx 0.7$). For lower temperatures the average nematic order increases in the systems, at the same time the radii of the Saturn rings decrease (see Figure 5.10), which is in agreement with experiments [21].

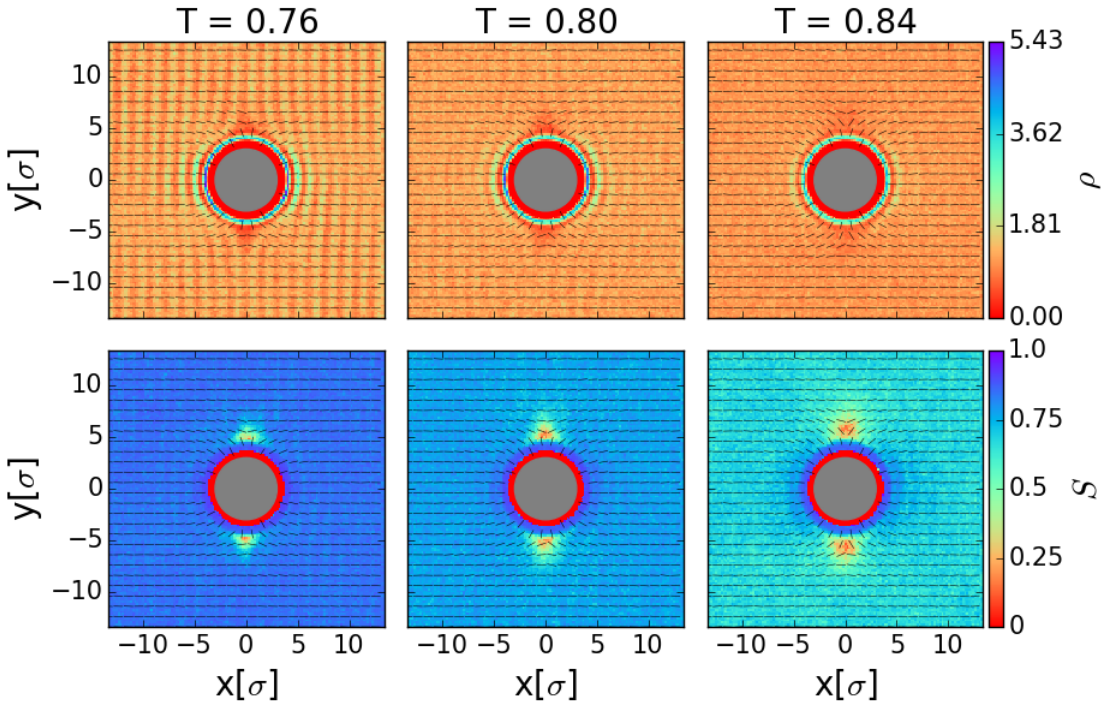

Figure 5.9: Filed maps of systems with a colloidal inclusion and homeotropic anchoring with anchoring parameters $\epsilon_{\mathrm{mc}} = 1\epsilon_0$ and $\eta = 0.5\sigma^{-1}$ at different temperatures T and visualized on a centered cross section. The figures in the upper row show the particle density field ρ, the figures in the lower row show the nematic order field S. The small black bars depict the orientation of the local director.

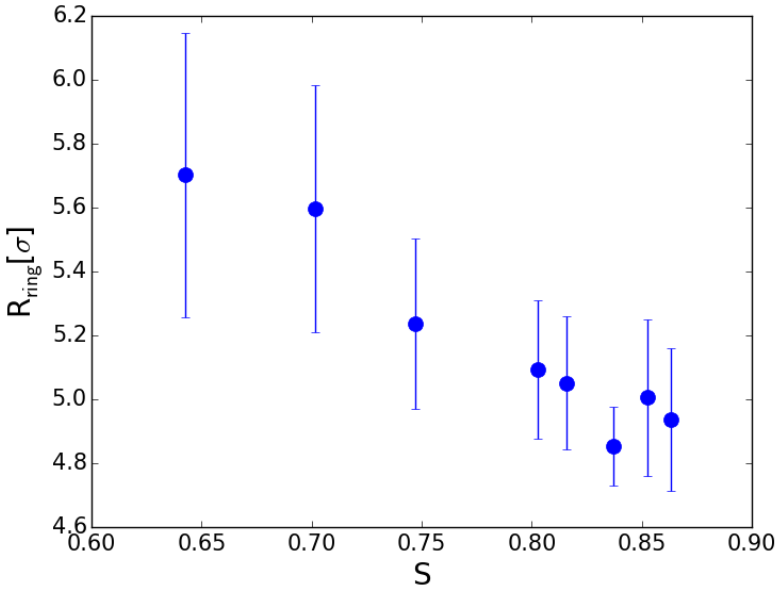

Figure 5.10: Dependence of the Saturn ring radius on the global nematic parameter S.

In the nematic systems, the particle density is for the most part homogeneous, apart from fluctuations. Close to the colloid, however, there is a shell of roughly one LC particle length in thickness where the particle density can be up to three times larger than the density further away from the colloid.

Contrary to experimental observations [21], the Saturn ring is also present in the smectic A phase for temperatures below $T \approx 0.78$. In contrast to the nematic systems at higher temperatures, the cross sections of the rings become less diffuse and more triangular in shape. Comparing with the density field around the colloid, the Saturn ring coincides with a region of low density, also of roughly triangular cross-section. In this region the distance between adjacent particle layers is especially high, as they bend around different hemispheres of the colloid. Inside this gap, LC particles are able to rotate with relative ease, as neither interactions with the colloid nor the interactions with the surrounding layers of LC particles are dominant there.

The inverse screening length is set to $\eta = 5\sigma^{-1}$, letting the interaction potential U_{mc} to decay on a much shorter length scale and resulting in an effectively weaker anchoring. In the nematic phase, the colloids are again encircled by a defect ring, just as in the systems with smaller η (see Figure 5.11). Compared to the latter, however, the defect ring is a lot more diffuse and its radius is a bit smaller. This is also true in the smectic A phase where we are still able to observe the formation of a defect ring. This region of low nematic is located just at the surface of the first shell of LC particles surrounding the inclusion, but now, the defect ring is sharper than in the case of $\eta = 0.5\sigma^{-1}$. At this value of η, the smectic layers are barely deformed by the presence of the colloid, thus preserving approximately equidistant

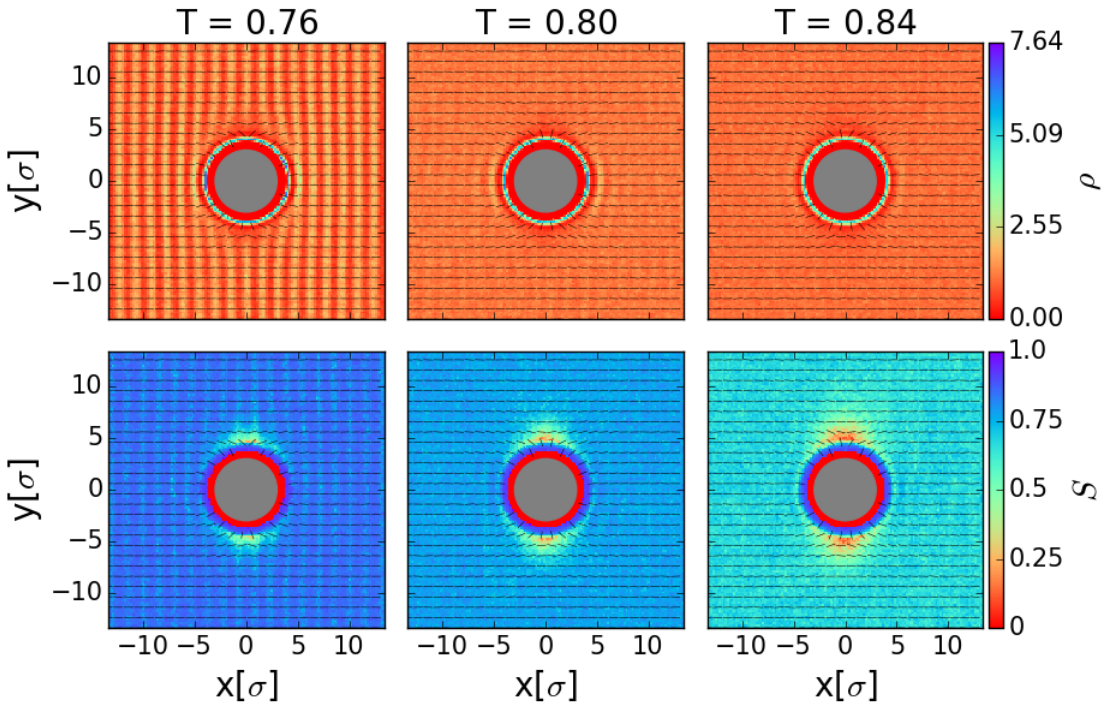

Figure 5.11: Cross sections of systems with a colloidal inclusion and homeotropic anchoring with anchoring parameters $\epsilon_{\mathrm{mc}} = 1\epsilon_0$ and $\eta = 5\sigma^{-1}$ at different temperatures T. The figures in the upper row show the field map of the density ρ, the figures in the lower row show the nematic order field S. The small black bars depict the orientation of the local director.

layers spacing. Nevertheless, the systems show no signs of the formation of focal line defects.

We carried out similar simulations for a larger system with 7×10^4 LC particles and one colloid with radius $R_{\mathrm{c}} = 6\sigma$ at a temperature of $T = 0.74$. This time we strenghten the anchoring by reducing the inverse screening lenght to $\eta = 0.05\sigma^{-1}$. The results are shown in Figure 5.12. Now, a second concentric shell of particles forms around the colloid. This kind of multilayerd and concentric structure is known as onion structure. It has been observed in lyotropic LCs where it can form under shear flow [49, 50]. Formation of onion structure has been observed in microchannels [51]. But as far as we know, these structures have not yet been reported for computer simulations or for colloidal inclusions.

5.5.2 Planar anchoring

When using the same anchoring parameters as in the case of homeotropic anchoring ($\epsilon_{\mathrm{mc}} = 1\epsilon_0$, $\mu = 0.5\sigma^{-1}$), for all temperatures we see that the director field is not everywhere aligned parallel with the colloid's surface, contrary to what one might expect from the anchoring function. Close to the equator of the colloid, the director

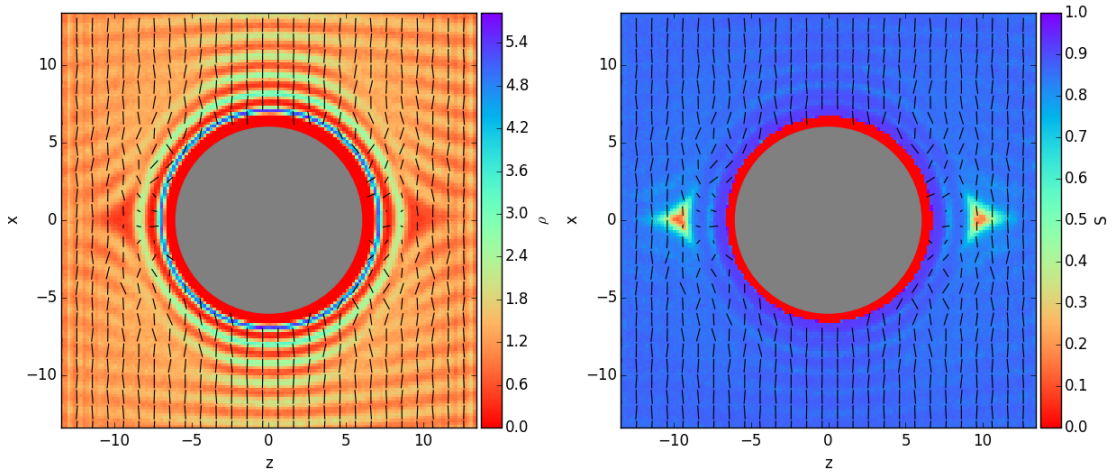

Figure 5.12: ross sections of systems with a colloidal inclusion and homeotropic anchoring with anchoring parameters $\epsilon_{\mathrm{mc}} = 1\epsilon_0$ and $\eta = 0.05\sigma^{-1}$. At this anchoring strength layers of particles further away from the colloid are bent around, forming a second 'onion' shell around the inclusion.

field at the surface of the former aligns parallel to it. But for larger latitudes (roughly for $\Theta > 30°$), the relative alignment changes and the anchoring becomes effectively perpendicular in the vicinity of the colloid's poles. Roughly at the latitude of the transition, a band of reduced nematic order is observed just above the colloids surface, in which the nematic order can even fall bellow $S = 1/3$, indicating isotropy. Interestingly enough, in the nematic phase, the nematic order is slightly increased at the colloids poles, even though the director field's alignment there is in opposition to the anchoring function. Also the nematic order for latitudes smaller than $\Theta \approx 60°$, the nematic order is slightly reduced even though the anchoring conditions are roughly in accordance with the global director. In the nematic and in the smectic A phases, the particle density is elevated at the poles. In the smectic A phase, the shape of the particle layers is barely influenced by the presence of the colloid. Only the layers touching the colloid's poles seem to bend very slightly towards the inclusion.

It is evident, that with this choice of anchoring parameters, the interaction between colloid and LC particles is not strong enough in order to align the particles planar at the poles, opposing the global director. This is not too surprising, as perpendicular alignment at a surface is entropically more favorable than parallel alignment. This property has also been observed in an initial stage of this thesis, when trying out different strengths for the LC particle-wall interaction. Despite planar anchoring, LC particles would align perpendicular to the walls if ϵ_{mw} was chosen too small. Consequently, the alignment of the LC particles close to the colloid is primarily dominated by interactions with the surrounding LC, resulting in

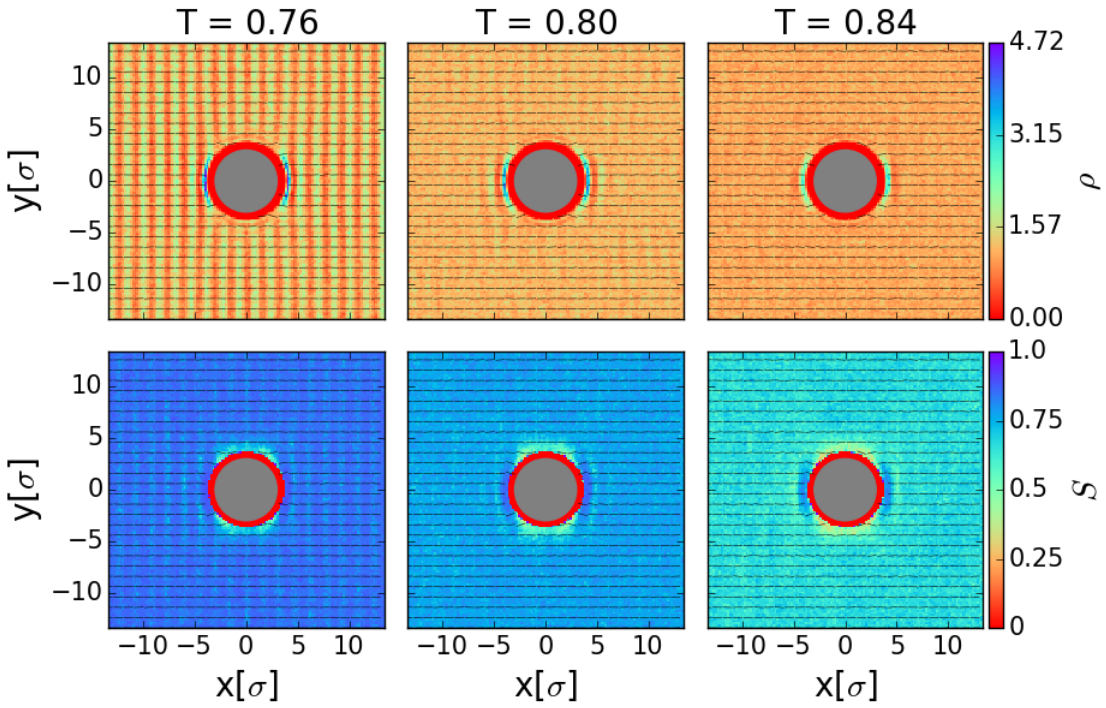

Figure 5.13: Cross sections of systems with a colloidal inclusion and planar anchoring at different temperatures T. The figures in the upper row show the particle density field ρ, the figures in the lower row show the nematic order field S. The small black bars depict the orientation of the local director.

an effective homeotropic anchoring close to the poles. The surface defects, the rings of reduced nematic order, form in the area in which the intrinsic planar anchoring transitions to effective homeotropic anchoring, leading to orientational frustration in this region and formation of a defect, akin to formation of ring defects around Janus colloids [48, 52].

For an interaction strength of $\epsilon_{\mathrm{mc}} = 3.5\epsilon_0$ and an inverse screening length of $\eta = 1.0\sigma^{-1}$ we observe the formation of two Boojum defects, discernible as regions of low nematic order at the colloid's poles (poles with respect to the global director $\hat{\mathbf{n}}_0$). In the cross sections of the systems, the director field within these regions (see Figure 5.14) exhibits the structure of -1/2 point defects. The appearance of this kind of defects is in agreement with previous theoretical and experimental work [16, 22, 32, 48]. Unlike in the simulations with homeotropic anchoring conditions, the colloids here are not enclosed by a region of high nematic order. The regions of reduced nematic order, corresponding to the Boojum defects, seem to reach down to the surface of the colloids. This also indicates that the director field at the colloid's surface has some discontinuities, even though this is not necessarily apparent from Figure 5.14. Discontinuities in the director field, right at the surface of the colloid

would be expected by virtue of the hairy ball theorem [53]. Only at the sides of the colloid, and only at larger temperatures (e.g. at $T = 0.84$) the nematic order becomes slightly larger than in regions farther away from the inclusion.

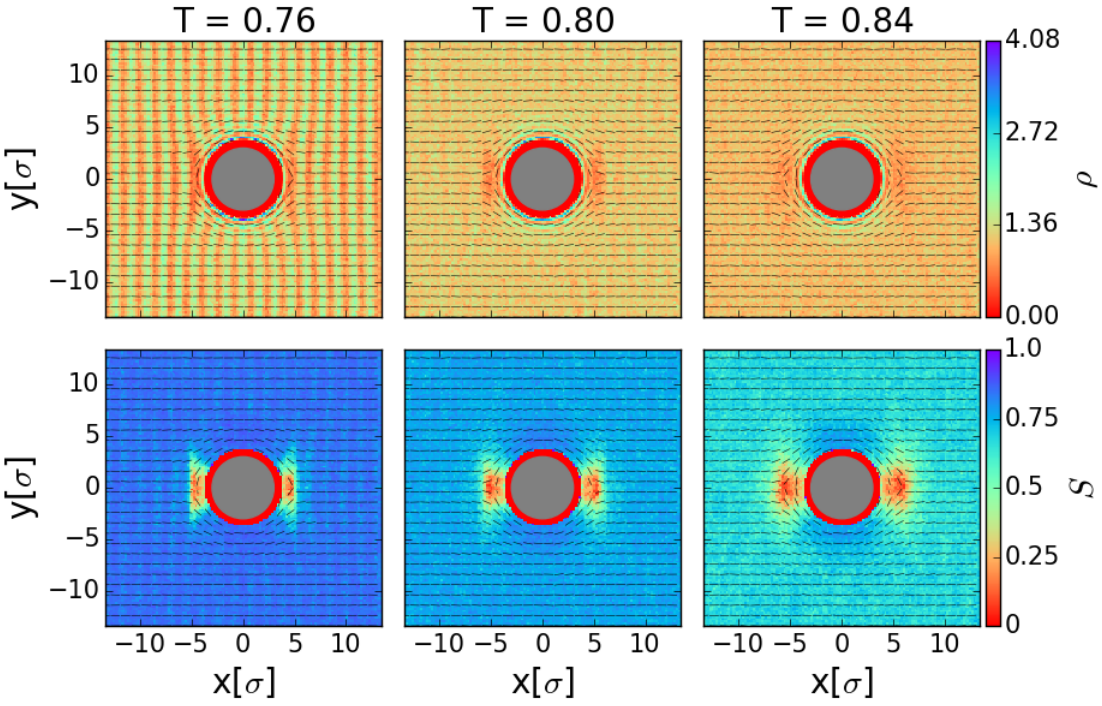

Figure 5.14: Cross sections of systems with a colloidal inclusion and strong planar anchoring at different temperatures T. The figures in the upper row show the particle density field ρ, the figures in the lower row show the nematic order field S. The small black bars depict the orientation of the local director.

The particle density close to the colloid's surface is again up to two or three times higher than in regions far away. But in contrast to the case with homeotropic anchoring, this shell is thinner (its thickness being about $d \approx 0.4\sigma$). As the temperature decreases the global nematic order increases, the defect's areas in the cross section become smaller and less diffuse. However, the defects still exist in the smectic A phase, which is at variance with experimental observations of colloidal inclusions in 8CB [22]. In the smectic A phase, the particle layers bend in the vicinity of the colloid, in order to align planar with the colloid's surface, thereby varying the inter layer spacing and leaving areas of low density at the colloid's poles. The defects, or regions of low nematic order, coincide with these gaps. In contrast to this, experimental results [22] show the vanishing of the Boojum defects and the appearance of a certain kind of defect lines, which are identified as focal lines.

The disagreement between experiments and the simulations of the present model essentially stems from the fact that the interactions of the model are weak enough

to allow the distance between adjacent layers to vary. However, we do not exclude the possiblity that for some LC materials the defect topologies found here might be realized.

5.6 Interaction of colloid pairs

After having looked at the influence of a single colloidal inclusion on the density- and director-field of the LC, the next step is to study systems containing pairs of colloids. Following the previous section, the density-, order and director-fields around stationary colloids are inspected, for both anchoring types as well as for different alignments of the colloids with respect to the global director. Additionally, several systems are observed, in which the colloid pairs are allowed to move freely. With these observations we want to inspect whether the LC mediates an effective inter-colloidal interaction.

5.6.1 Homeotropic anchoring

We simulate a series of systems each containing 25×10^3 LC particles and a pair of colloids with fixed positions. The initial conditions of the systems are prepared such that colloids are always located in the x-y-plane at $z = 0$, symmetrically with respect to the center of the simulation box. The axis along which the colloids are aligned makes an angle ϕ with the x-axis. We set up systems with angles between $\phi = 0°$ and $\phi = 90°$ in steps of $\Delta\phi = 10°$. Each colloid has a radius $R_c = 3\sigma$ and the inter-colloidal center-to-center distance is $r_{cc} = 9\sigma$. Continuous walls with planar anchoring are introduced parallel to the x-y-plane on top and on the bottom of the simulation box in order to stabilize the LC particles' orientations along the x-axis. The simulations are carried out for the smectic A phase at pressure $P = 1.0$ and temperature $T = 0.76$.

Cross sections of the system at $z = 0$ showing the field maps for density, nematic order parameter and local director are depicted in Figure 5.15 for some angles ϕ. Portrayals of the full three dimensional structure of the defects around the colloids are shown in Figure 5.16. For small alignment-director angles (roughly $\phi < 50°$) the systems look like two separate single-colloid systems were put next to each other (compare for example with Figure 5.9). Each colloid is encircled by a defect ring, winding around its equator. The rings can be seen in the cross sections of the nematic order fields in Figure 5.15 as the roughly triangular-shaped regions of reduced nematic order. The director field in the vicinity of these regions looks like a -1/2 defect, as it is expected of a Saturn ring defect. In the same figure it can be seen, that these regions coincidentally feature a low particle density. At larger angles ($\phi > 60°$), the defect rings are deformed, such that they do not fully lie in the colloids' equatorial planes anymore. This deformation indicates the mutual interaction of the defect lines. The colloids' interaction with the LC particles ensures that the former are surrounded by a shell of finite thickness, in which the LC particles are

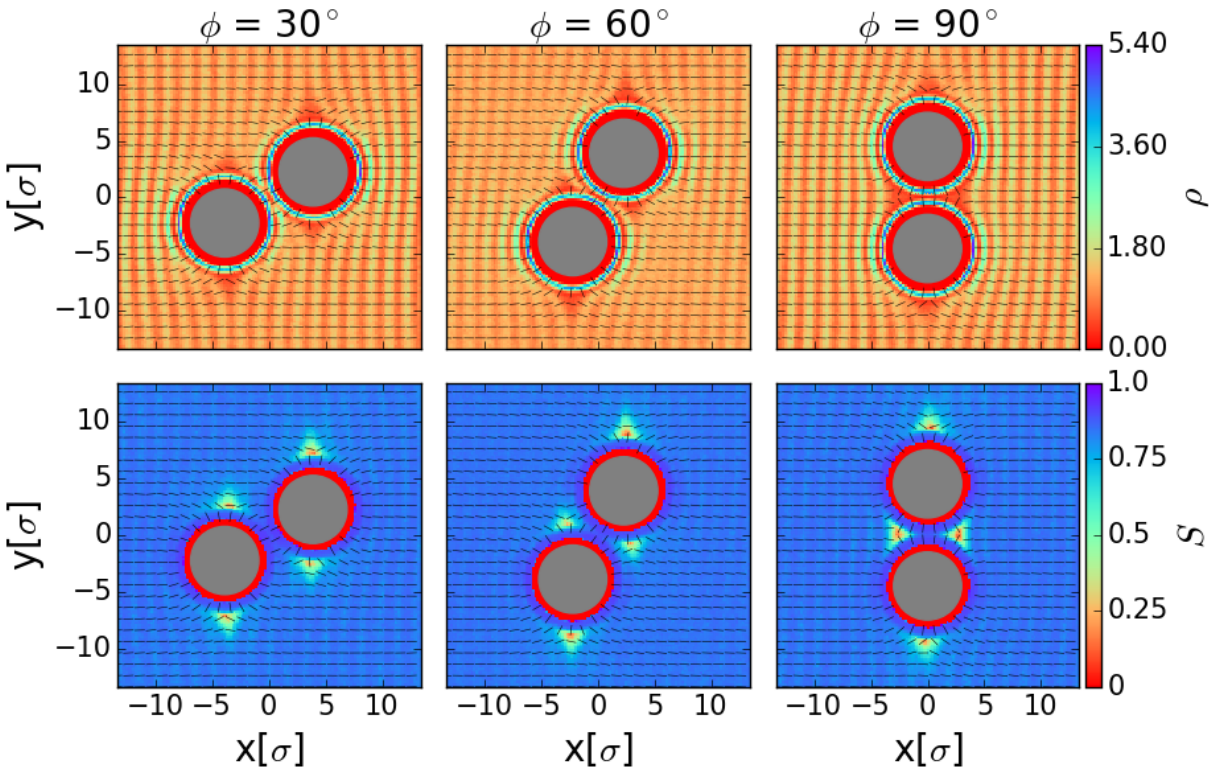

Figure 5.15: Density field ρ, nematic order field S and director-field in the x-y-plane around the colloids at different alignment angles ϕ with the global director.

oriented perpendicularly to the colloid's surface. The defect rings must be located just outside this shell. As the angle ϕ increases, the ring around one colloid is pushed aside by the other colloid's 'nematic shell'. Eventually when the colloids make an angle of close to $\phi = 90°$ with the global director, the defect rings merge to a single structure.

5.6.2 Freely moving colloids

In order to study freely moving pairs of colloids, a series of systems is prepared just like for the simulation of static colloid configurations (see section 5.6.1): colloids of radius $R_c = 3\sigma$ are placed in the x-y-plane, symmetrically with respect to the simulation box' center with angles $\phi \in [0°, 90°]$ in steps of $\Delta\phi = 10°$ with an inter-colloidal distance of $r_{cc} = 3\sigma$. Continuous walls with planar anchoring stabilize the global director along the x-axis. During the equilibration, the positions of the colloids are kept fixed. After equilibration, the colloids are allowed to move freely, only interacting with the LC particles according to equation (3.30) and interacting with the other colloid according to the fully repulsive potential $U_{cc} = \epsilon_0(\sigma/r_{cc})^{10}$. Inter colloidal interactions are cut-off beyond a cut off distance of $r_{cc} = 6\sigma$. The

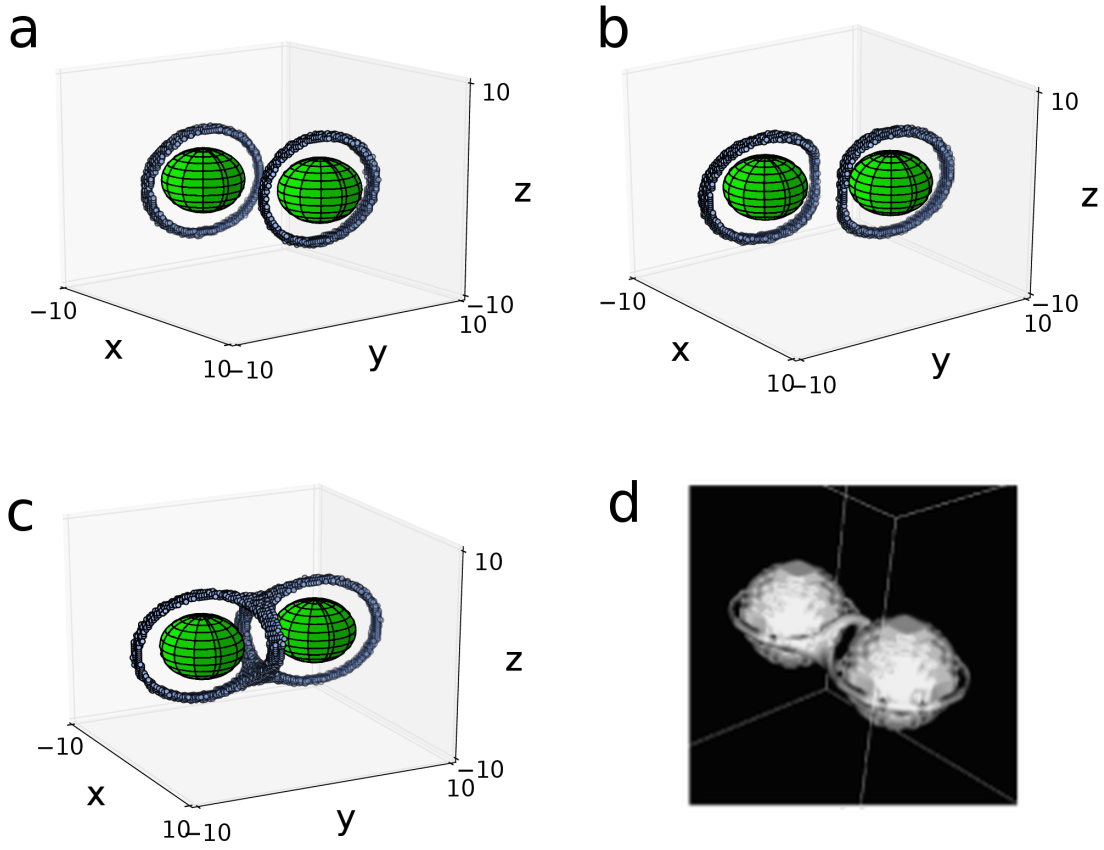

Figure 5.16: Visualization of the defect rings around both colloids. (a) The colloids are aligned along the global director ($\phi = 0°$), the defect rings can be approximated by simple rings located in the equatorial planes of their respective colloids. (b) The alignment of the colloids make an angle of $\phi = 60°$ with the global director. The defect rings are clearly deformed. (c) The colloids' alignment makes an angle $\phi = 90°$. The defects merge to a single structure. (d) Comparison with numerical results fro a nematic system, image taken from citeguzman2003defect.

positions of the colloids as well as the global director are recorded over the course of the simulations. These data are used to reconstruct the evolution of the inter-colloidal distance r_{cc} as well as the evolution of the angle ϕ (see Figure 5.17).

Except for two simulations, one which started from an angle $\phi = 20°$ and one which started from an angle $\phi = 10°$, all simulations eventually end up in a similar configuration: the colloids remain at a distance $r_{cc} \approx 2.8\sigma$ away from each other and they tend to align roughly perpendicular to the global director (the value of ϕ falls approximately between $\phi = 80°$ and $\phi = 90°$). However, colloids starting from an angle smaller than $\phi = 60°$ tend to move away from each other initially, while the angle ϕ tends to grow quite fast until it reaches values of about $\phi = 50°$ or $\phi = 60°$. Colloids starting at lower angles ϕ can drift quite far apart from each other, $r_{cc} = 6\sigma$ or more, before they approach each other again. It is therefore not clear whether they really attract each other at such distances or if they randomly drift about until they coincidentally get close enough to interact. Interestingly enough, there seems to be a certain distance $r_{cc} \approx 4\sigma$ at which colloid pairs, which started at angles smaller or equal than $\phi = 70°$ may remain for some time. They eventually change to a distance of $r_{cc} \approx 2.8\sigma$ and this rearrangement happens quite abruptly. Considering, that the inter-colloidal interaction as given by the potential U_{cc} is purely repulsive, this behavior points towards an effective anisotropic interaction, which is mediated by the LC host phase.

Expecting the configurations of sticking colloids at $\phi = 90°$ to be energetically favorable we look at the time-averaged total potential energy between the LC particles U_{mm} (see Figure 5.20), at the average potential energy between colloids and LC particles U_{mc} (see Figure 5.21) and at the splay, twist and bend distortions[1] (see Figure 5.19), all obtained from the simulations with static colloids (see section 5.6.1). In the vein of [16] we also look at the defects' volume, the combined volume of regions of low nematic order around the defects (see Figure 5.18), as these contribute positively to the energy of the system.

The results of the combined defect volume seem to exhibit a local minimum for configurations in which the colloids and the director make an angle of $\phi = 30°$. The combined defect volume makes a jump when going from an angle $\phi = 80°$ to $\phi = 90°$ where it actually assumes its largest value. The size of the combined defect can therefore be excluded as a possible source of the interaction between the colloids, as that would require a minimum at large angles. For the same reason, the colloid's interaction cannot be attributed to the elastic energies of the director field, as the distortions also become maximal for an angle of $\phi = 90°$. Looking at average potential energy between the LC particles, it seems as if it has a slight tendency to be smaller at larger angles. With the current statistics, however, it is not possible to tell whether this is an actual trend or just a coincidence, as the variance of the data is so large. The results of the average energy between the LC particles and the colloids show a clear trend which displays a minimum at large angles, roughly at

[1] The actual values of the distortion free energy cannot be calculated, as the elastic constants are unknown for the smectic phase.

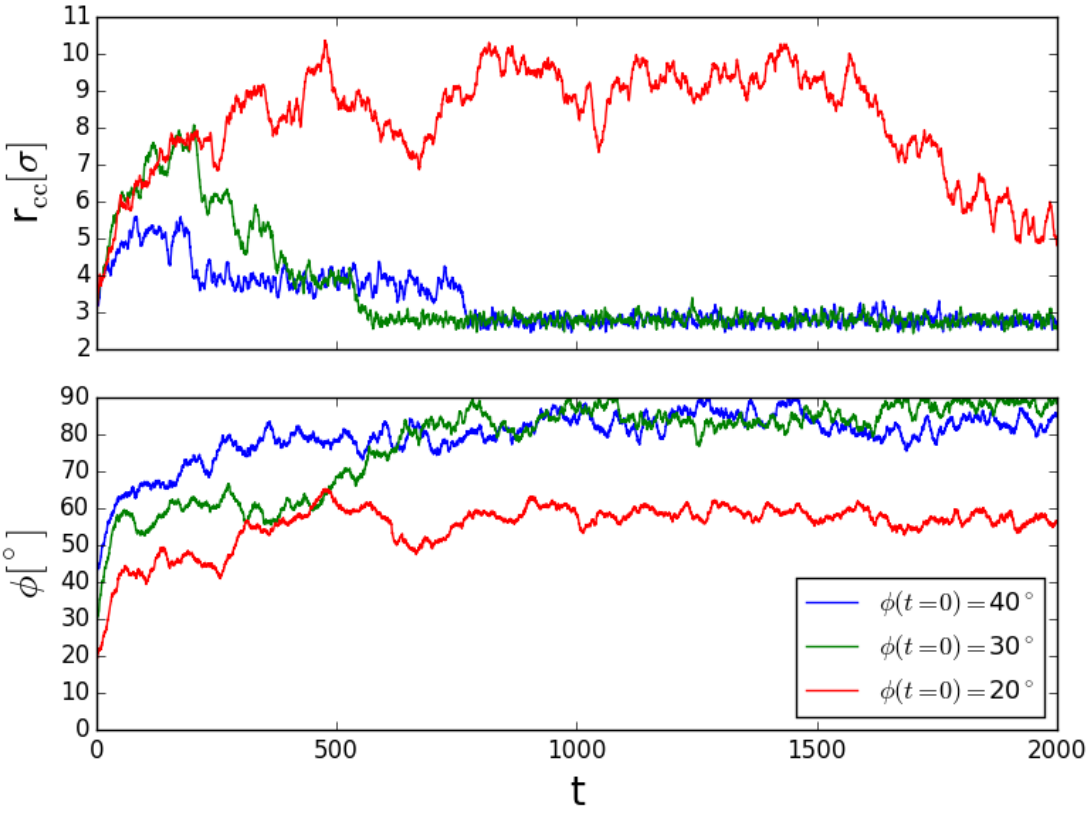

Figure 5.17: Time evolution of the inter-colloidal distance r_{cc} and angle ϕ for three different initial conditions. The behaviour shown by the simulations starting at $\phi(t = 0) = 30°$ and at $\phi(t = 0) = 40°$ are exemplary for most of the simulations. Only two simulations (one of them starting from $\phi(t = 0) = 20°$) do not end up in a simular configuration by the end of their run time.

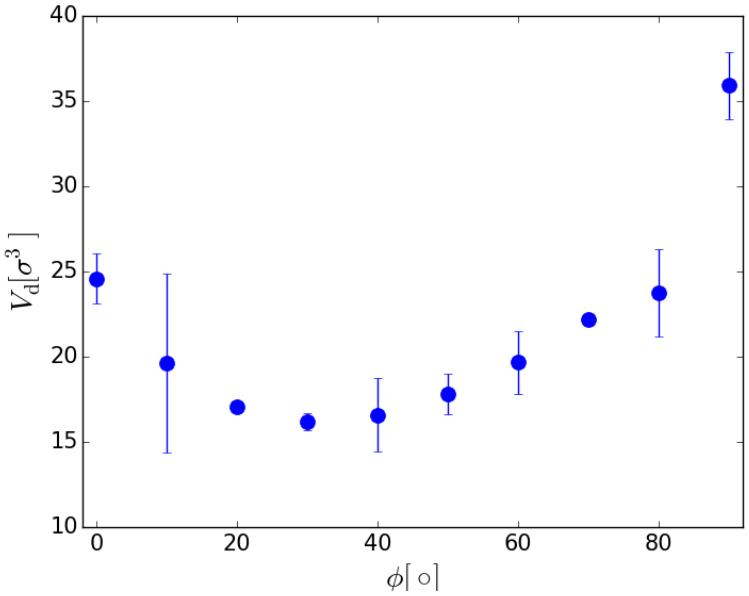

Figure 5.18: Combined volume occupied by the defect structures surrounding both colloids.

$\phi = 80°$. However, the absolute values of these are minuscule, compared for example to the average potential energies between the LC particles.

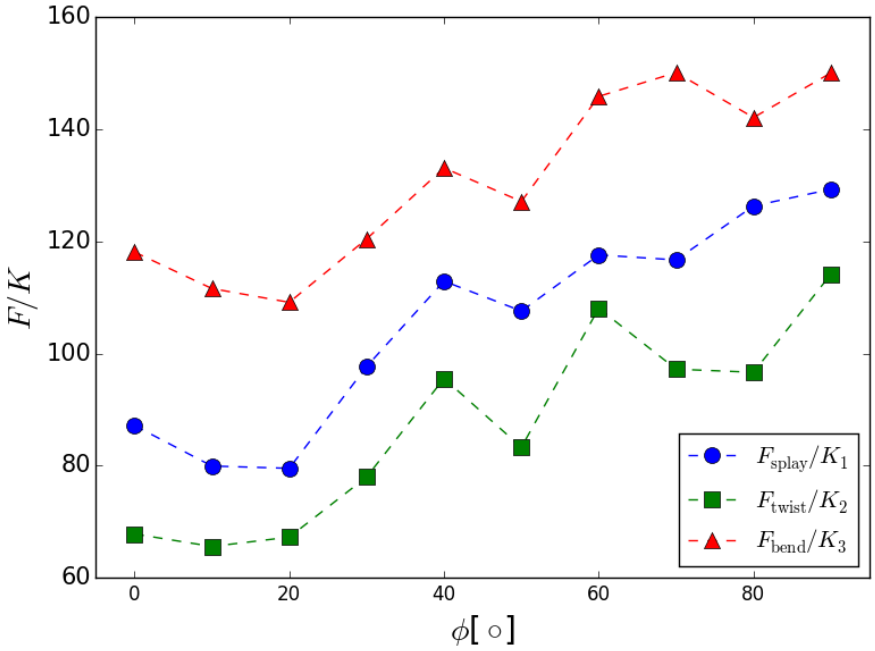

Figure 5.19: Splay, twist and bend, averaged over the whole system, in dependence of the angle ϕ between the global director and the axis connecting both colloids.

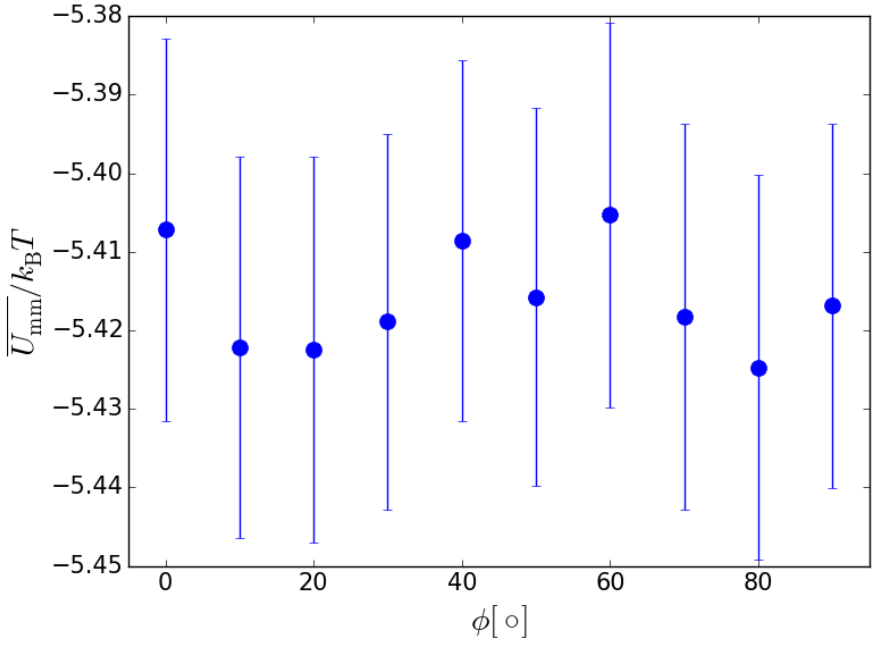

Figure 5.20: Average potential energy between LC particles depending on the angle ϕ between the global director and axis connecting both colloids.

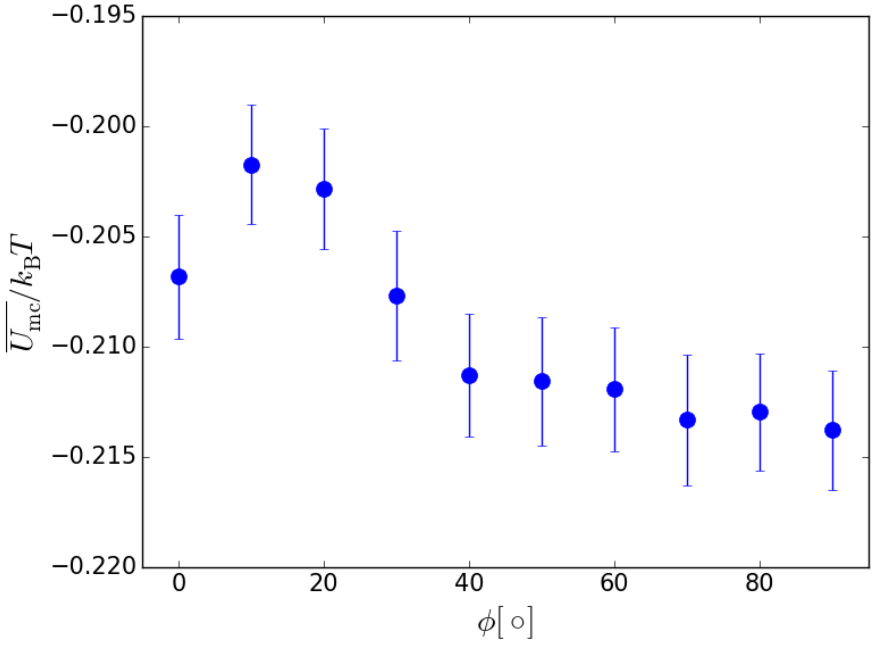

Figure 5.21: Average potential energy between LC particles and the colloids depending on the angle ϕ between the global director and axis connecting both colloids.

6 Summary and conclusion

A simple model for LC particles is studied numerically by means of MD simulations. It is found that the model is capable of forming stable isotropic, nematic as well as smectic A phases. At pressure $P = 1.0$ the transition from the isotropic to the nematic phase is observed at $T_{\mathrm{IN}} \approx 0.87$, the nematic smectic A transition is observed at $T_{\mathrm{NSmA}} \approx 0.78$. The self-diffusion in the bulk phase is studied by considering the MSDs of the LC particles parallel and perpendicular to their orientations. For large observation times, the MSDs reveal diffusive behaviour. In the smectic A phase, the MSD along the LC particles' orientations shows a subdiffusive behaviour for intermediate observation times, which indicates the one-dimensional crystal-like structure of this phase. The three different phases can be distinguished by the temperature dependence of the diffusion coefficients which are estimated from the MSD. In the isotropic phase, the diffusion coefficient $D_{\parallel}$ along the particles' orientations is practically indistinguishable from the diffusion coefficient $D_{\perp}$ perpendicular to their orientations, as one would expect. In the nematic and in the smectic A phase self-diffusion becomes anisotropic with $D_{\perp} < D_{\parallel}$ throughout the higher temperature range of the nematic phase and $D_{\parallel} < D_{\perp}$ in the smectic A phase.

The splay, twist and bend elastic constants of model's director field are estimated from the fluctuations of the Fourier transformed nematic order tensor in the nematic phase. The elastic constants turn out to decrease monotonically with increasing temperature. For temperatures $T > 0.82$ the three elastic constants assume roughly the same value. As the temperature approaches the nematic smectic A transition the twist and bend elastic constants grow strongly, leading one to believe they might even diverge at the onset of the smectic phase. However, later results from the study of colloidal inclusions indicate that this might not be the case. Compared to those the splay elastic constant grows roughly linear with decreasing temperature, definitely remaining finite. Qualitatively, the behaviour of the elastic constants is comparable to that of octylcyanobiphenyl (8CB). The studied model might thus be suitable for approximating this kind of LC, at least in the nematic phase.

The effect of a colloidal inclusion on the model LC's director field is studied. Due to the incompatibility of the uniform director field imposed by the systems boundary conditions, with the radial symmetry of the colloid, defects in the director field arise. For homeotropic surface anchoring of the colloid, a Saturn ring defect is formed around the colloid, as is expected from theory and experiments. The radius of the Saturn ring is observed to shrink with decreasing temperature and increasing global nematic order. The Saturn rings persist in the smectic A phase, within an anular region of low density which forms due to deformation of the smectic layers around the colloid.

In case of planar anchoring at the colloid's surface, the interaction strength and range need to be higher, compared to those in the homeotropic case, in order to be able to observe the formation of two point-like Boojum defects at the colloid's poles. In the smectic A phase, the defects at the poles are also present. The layers which are intersected by the colloid are bent, aligning almost perpendicular to the colloid's surface, creating two regions of low density in which the defects are located. For interaction strength and range comparable to the case of homeotropic anchoring, the interaction is too weak to align the LC particles at the colloid's poles with its surface, resulting in an effective homeotropic anchoring, close to the poles. For that reason, no Boojum defects are observed in these systems. However two defect rings can be observed forming almost at the colloid surface, where the effective intrinsic planar anchoring transitions into effective homeotropic anchoring close to the colloid's. The formation of experimentally observed focal defects is not observed in our simulations. The principal reason for that is that the spacing of our models' smectic layers is not equidistant everywhere, letting deformation of the smectic layers decay rapidly within small distances. The lack of equidistant layering is a feature inherent to the model as it might result from the repulsion of LC particles in the end-to-end configuration, which prevents a stable and finite inter particle distance. This might also lead the bend elastic constant to have a finite value in the smectic A phase

The defect structures induced by pairs of colloids with homeotropic anchoring generally depend on the colloid's distance but also on their mutual orientation with respect to the system's global director. If the angle ϕ enclosed by the global director and the line, joining both colloids, is smaller than $\phi = 50°$ or $\phi = 60°$, each colloid is surrounded by a simple Saturn ring defect. For larger angles the rings start to deform. For angles $\phi > 80°$ both defect rings combine into a single triple-ring structure. This sort of structure has previously been reported for simulations of a nematic LC by Guzmán et al. [54] and has also been treated theoretically [55]. Both colloids are left to move freely in the smectic A LC phase, starting at different angles ϕ most simulations end up with both colloids staying close to each other at an angle ϕ close to $\phi = 90°$, indicating that the LC mediates an effective attraction between the colloids. Considerations of defect sizes and energies indicate that the attraction might be dominated by interaction energy u_{mc} between the colloids and the LC particles as opposed to being elastically driven like other colloidal systems in nematic phases [16]. However, this is not conclusive, as the difference in potential

energy U_{mc} between configurations of high and low ϕ as of the same order of the energy fluctuation in the system.

There are still few open points which would be straightforward to investigate, but which, in the end, were not included in this thesis due to time constraints. Regarding the pair of colloids with homeotropic anchoring, this would involve the influence of the intercolloidal distance on the shape of the Saturn ring defects. Also the influence of their distance on their mutual attraction should be considered more carefully. Furthermore, the temperature and thus the nematic order paramter S should be varied, to see how this affects their interaction. The same investigation can also be performed for colloid pairs with planar anchoring of course. Also, the interactions between colloids of diffent anchoring types could be considerd.

In conclusion, the studied model produces nematic and smectic A phases and its bulk properties are qualitatively comparable to real LCs, most notably 8CB. The model might therefore lend itself for modeling these LCs to some extent, at least in the nematic phase. In the smectic A phase, the simulations of the model LC with inclusions fails to reproduce experimental results, most notably the formation of focal line defects. Furthermore, even though the model is computationally more complex than other simple models, as for example the model by Hess and Su [25], the model is simple enough that systems composed of about 7×10^4 particles can be simulated in a reasonable amount of time (roughly one week).

7 Appendix

7.1 Phase diagram

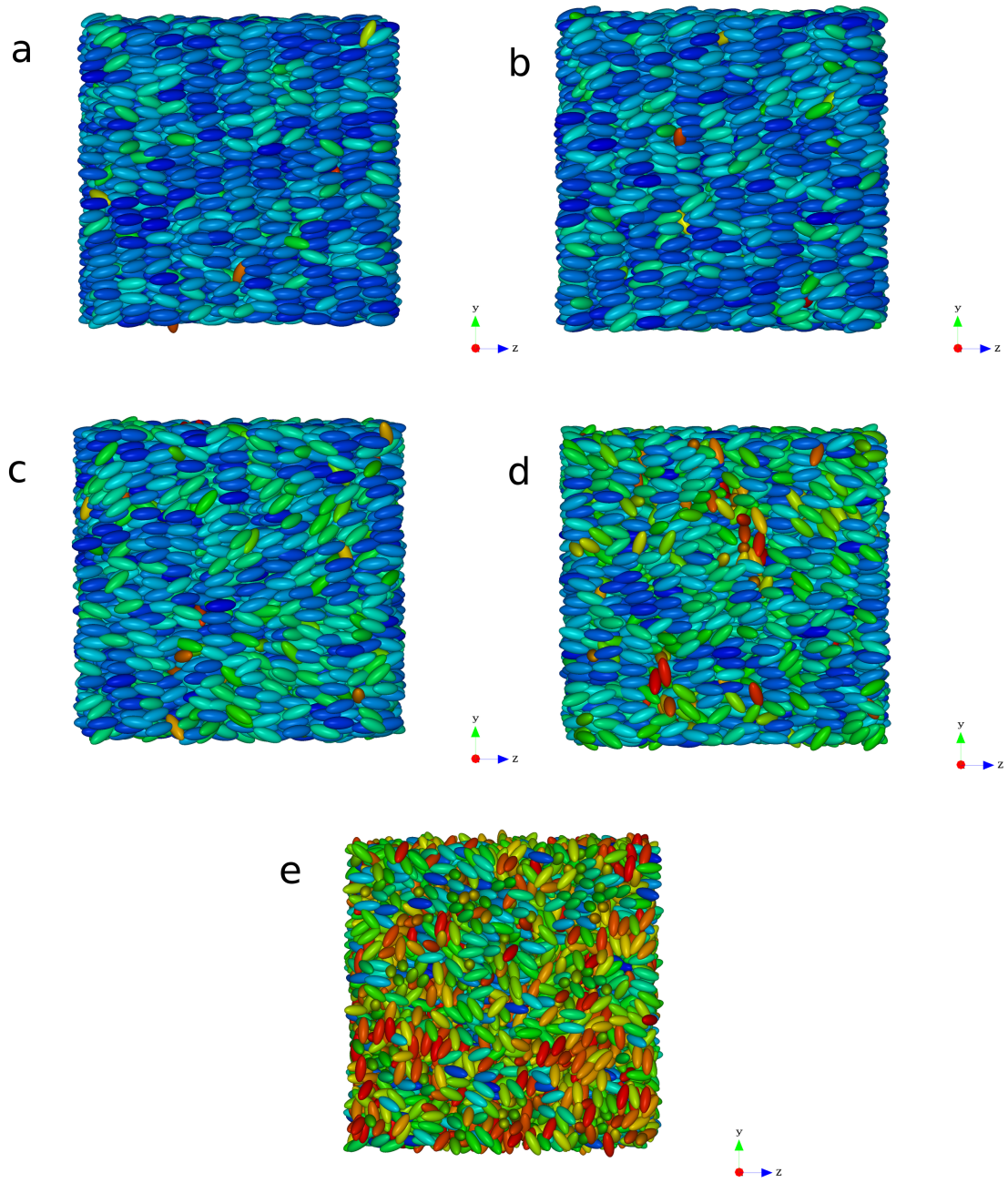

Figure 7.1: Visualizations of final configurations for systems with $N = 6000$ particles at $P = 1.0$ for various temperatures: (a) $T = 0.72$, (b) $T = 0.76$, (c) $T = 0.80$, (d) $T = 0.84$, (e) $T = 0.88$. The color of the particles indicates the deviation of its orientation from the global director $\hat{\mathbf{n}}_0$ in the system, dark blue meaning perfect alignment with $\hat{\mathbf{n}}_0$ and red meaning orthogonality with respect to $\hat{\mathbf{n}}_0$.

7.1.1 Temperature dependence of order parameters

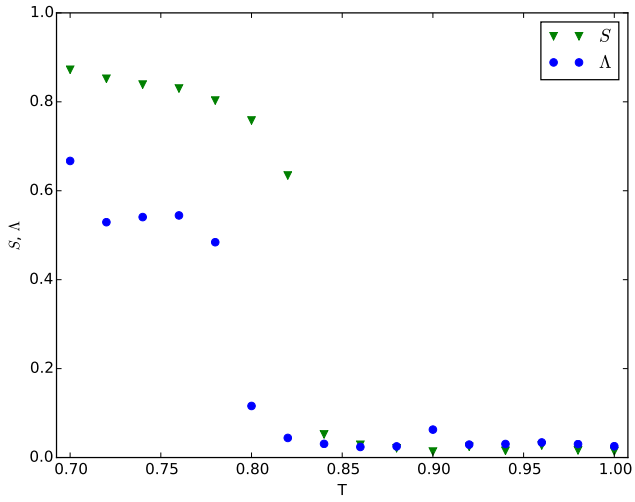

Figure 7.2: Temperature dependence of the nematic order parameter S and the smectic A order parameter Λ at pressure $P = 0.80$.

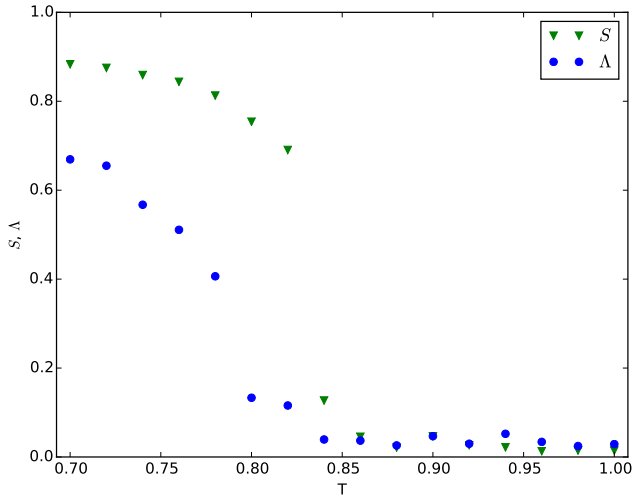

Figure 7.3: Temperature dependence of the nematic order parameter S and the smectic A order parameter Λ at pressure $P = 0.85$.

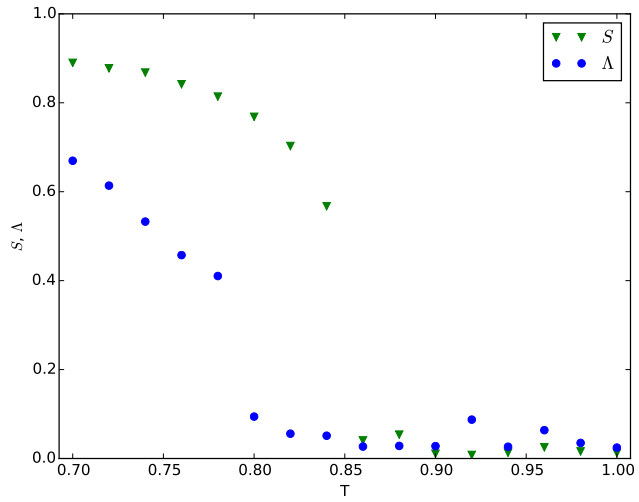

Figure 7.4: Temperature dependence of the nematic order parameter S and the smectic A order parameter Λ at pressure $P = 0.90$.

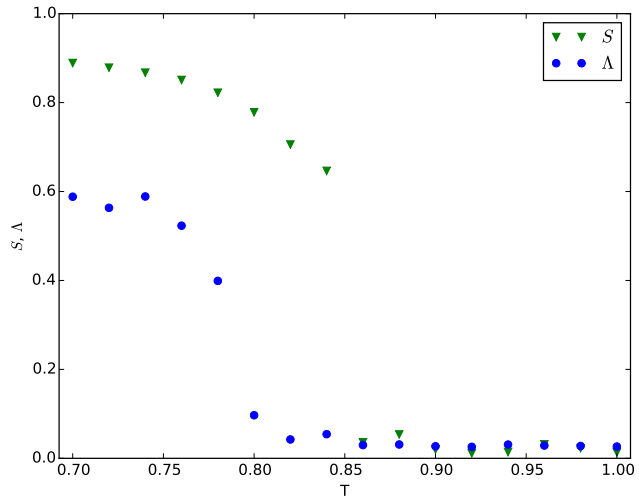

Figure 7.5: Temperature dependence of the nematic order parameter S and the smectic A order parameter Λ at pressure $P = 0.95$.

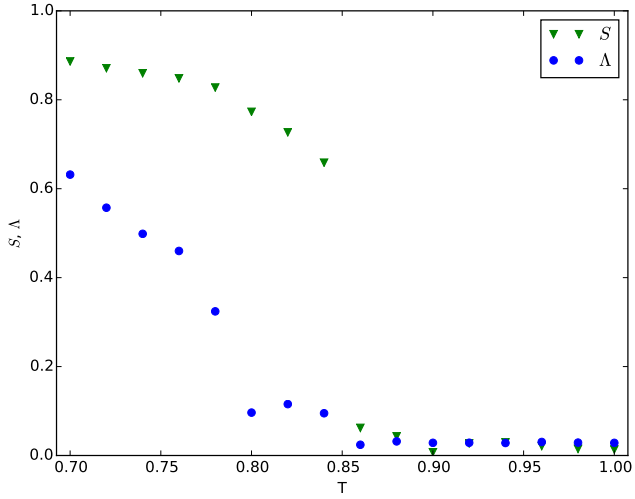

Figure 7.6: Temperature dependence of the nematic order parameter S and the smectic A order parameter Λ at pressure $P = 1.00$.

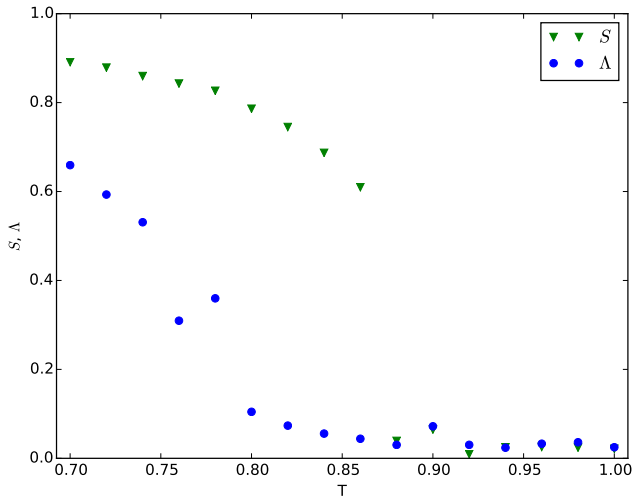

Figure 7.7: Temperature dependence of the nematic order parameter S and the smectic A order parameter Λ at pressure $P = l.05$.

7.2 Colloid-induced defects

7.2.1 Homeotropic anchoring

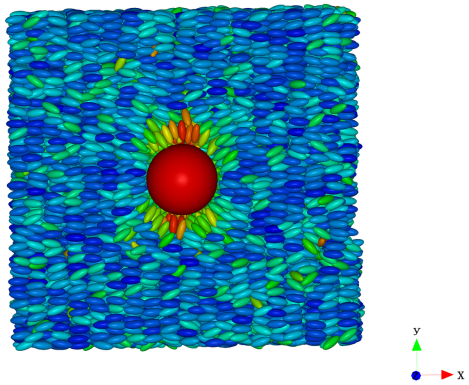

Figure 7.8: Visualizations of final configurations for a system with $N = 20000$ LC particles, $T = 0.76$ and a fixed colloid with homeotropic anchoring conditions with $\eta_{\mathrm{mc}} = 0.5\sigma^{-1}$. particles indicates the deviation of its orientation from the global director $\hat{\mathbf{n}}_0$ in the system, dark blue meaning perfect alignment with $\hat{\mathbf{n}}_0$ and red meaning orthogonality with respect to $\hat{\mathbf{n}}_0$.

7.2.2 Weaker homeotropic anchoring

7.2.3 Planar anchoring

7.2.4 Stronger planar anchoring

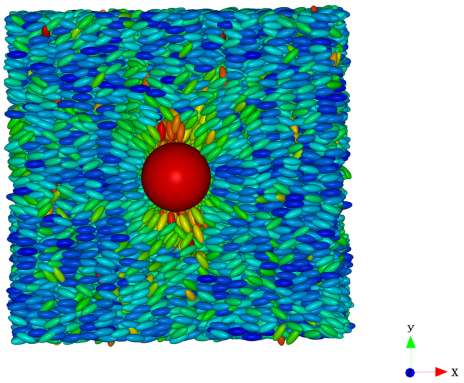

Figure 7.9: Visualizations of final configurations for a system with $N = 20000$ LC particles, $T = 0.80$ and a fixed colloid with homeotropic anchoring conditions with $\eta_{\text{mc}} = 0.5\sigma^{-1}$. particles indicates the deviation of its orientation from the global director $\hat{\mathbf{n}}_0$ in the system, dark blue meaning perfect alignment with $\hat{\mathbf{n}}_0$ and red meaning orthogonality with respect to $\hat{\mathbf{n}}_0$.

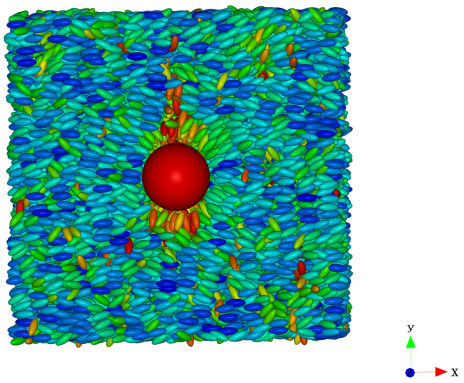

Figure 7.10: Visualizations of final configurations for a system with $N = 20000$ LC particles, $T = 0.84$ and a fixed colloid with homeotropic anchoring conditions with $\eta_{\text{mc}} = 0.5\sigma^{-1}$. particles indicates the deviation of its orientation from the global director $\hat{\mathbf{n}}_0$ in the system, dark blue meaning perfect alignment with $\hat{\mathbf{n}}_0$ and red meaning orthogonality with respect to $\hat{\mathbf{n}}_0$.

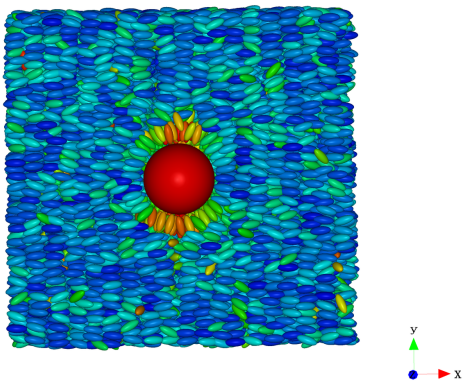

Figure 7.11: Visualizations of final configurations for a system with $N = 20000$ LC particles, $T = 0.76$ and a fixed colloid with homeotropic anchoring conditions with $\eta_{\text{mc}} = 5\sigma^{-1}$. particles indicates the deviation of its orientation from the global director $\hat{\mathbf{n}}_0$ in the system, dark blue meaning perfect alignment with $\hat{\mathbf{n}}_0$ and red meaning orthogonality with respect to $\hat{\mathbf{n}}_0$.

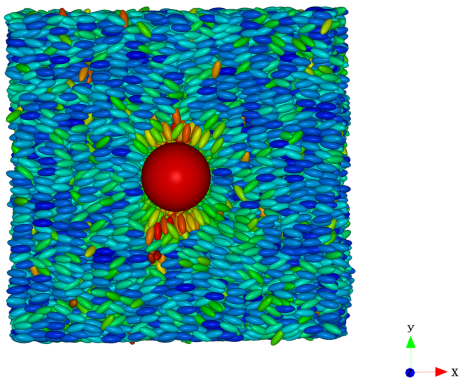

Figure 7.12: Visualizations of final configurations for a system with $N = 20000$ LC particles, $T = 0.80$ and a fixed colloid with homeotropic anchoring conditions with $\eta_{\text{mc}} = 5\sigma^{-1}$. particles indicates the deviation of its orientation from the global director $\hat{\mathbf{n}}_0$ in the system, dark blue meaning perfect alignment with $\hat{\mathbf{n}}_0$ and red meaning orthogonality with respect to $\hat{\mathbf{n}}_0$.

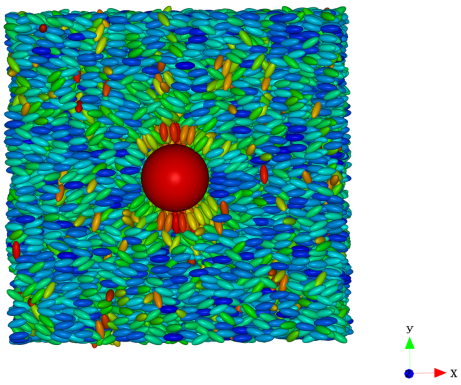

Figure 7.13: Visualizations of final configurations for a system with $N = 20000$ LC particles, $T = 0.84$ and a fixed colloid with homeotropic anchoring conditions with $\eta_{\text{mc}} = 5\sigma^{-1}$. particles indicates the deviation of its orientation from the global director $\hat{\mathbf{n}}_0$ in the system, dark blue meaning perfect alignment with $\hat{\mathbf{n}}_0$ and red meaning orthogonality with respect to $\hat{\mathbf{n}}_0$.

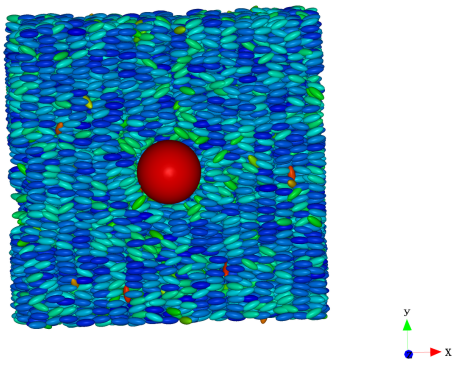

Figure 7.14: Visualizations of final configurations for a system with $N = 20000$ LC particles, $T = 0.76$ and a fixed colloid with planar anchoring conditions with $\eta_{\text{mc}} = 0.5\sigma^{-1}$. particles indicates the deviation of its orientation from the global director $\hat{\mathbf{n}}_0$ in the system, dark blue meaning perfect alignment with $\hat{\mathbf{n}}_0$ and red meaning orthogonality with respect to $\hat{\mathbf{n}}_0$.

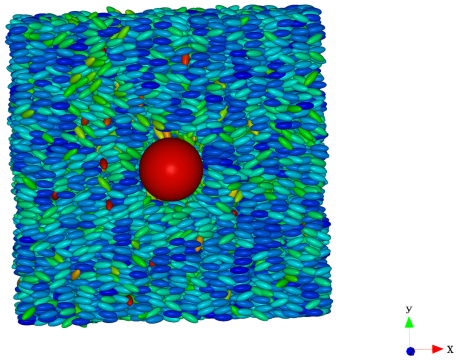

Figure 7.15: Visualizations of final configurations for a system with $N = 20000$ LC particles, $T = 0.80$ and a fixed colloid with planar anchoring conditions with $\eta_{\text{mc}} = 0.5\sigma^{-1}$. particles indicates the deviation of its orientation from the global director $\hat{\mathbf{n}}_0$ in the system, dark blue meaning perfect alignment with $\hat{\mathbf{n}}_0$ and red meaning orthogonality with respect to $\hat{\mathbf{n}}_0$.

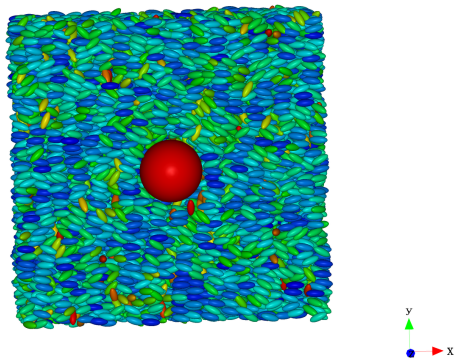

Figure 7.16: Visualizations of final configurations for a system with $N = 20000$ LC particles, $T = 0.84$ and a fixed colloid with planar anchoring conditions with $\eta_{\text{mc}} = 0.5\sigma^{-1}$. particles indicates the deviation of its orientation from the global director $\hat{\mathbf{n}}_0$ in the system, dark blue meaning perfect alignment with $\hat{\mathbf{n}}_0$ and red meaning orthogonality with respect to $\hat{\mathbf{n}}_0$.

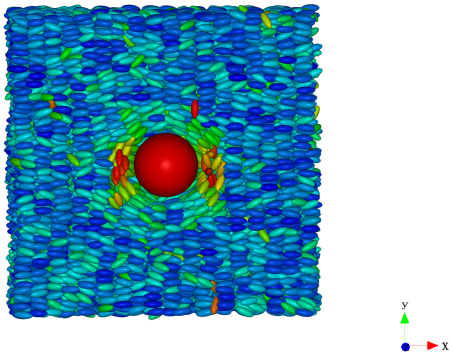

Figure 7.17: Visualizations of final configurations for a system with $N = 20000$ LC particles, $T = 0.76$ and a fixed colloid with planar anchoring conditions with $\eta_{\text{mc}} = 1.0\sigma^{-1}$ and $\epsilon_{\text{mc}} = 3.5\epsilon_0$. particles indicates the deviation of its orientation from the global director $\hat{\mathbf{n}}_0$ in the system, dark blue meaning perfect alignment with $\hat{\mathbf{n}}_0$ and red meaning orthogonality with respect to $\hat{\mathbf{n}}_0$.

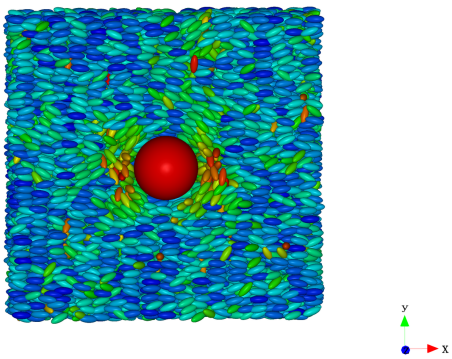

Figure 7.18: Visualizations of final configurations for a system with $N = 20000$ LC particles, $T = 0.80$ and a fixed colloid with planar anchoring conditions with $\eta_{\text{mc}} = 1.0\sigma^{-1}$ and $\epsilon_{\text{mc}} = 3.5\epsilon_0$. particles indicates the deviation of its orientation from the global director $\hat{\mathbf{n}}_0$ in the system, dark blue meaning perfect alignment with $\hat{\mathbf{n}}_0$ and red meaning orthogonality with respect to $\hat{\mathbf{n}}_0$.

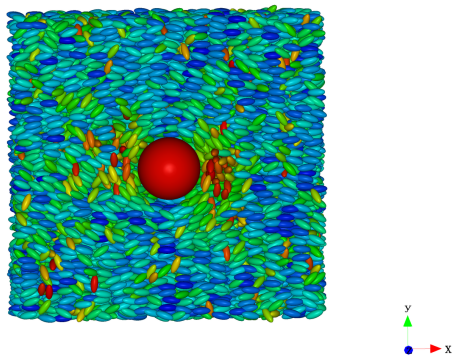

Figure 7.19: Visualizations of final configurations for a system with $N = 20000$ LC particles, $T = 0.84$ and a fixed colloid with planar anchoring conditions with $\eta_{\text{mc}} = 1.0\sigma^{-1}$ and $\epsilon_{\text{mc}} = 3.5\epsilon_0$. particles indicates the deviation of its orientation from the global director $\hat{\mathbf{n}}_0$ in the system, dark blue meaning perfect alignment with $\hat{\mathbf{n}}_0$ and red meaning orthogonality with respect to $\hat{\mathbf{n}}_0$.

7.3 Interaction of colloid pairs

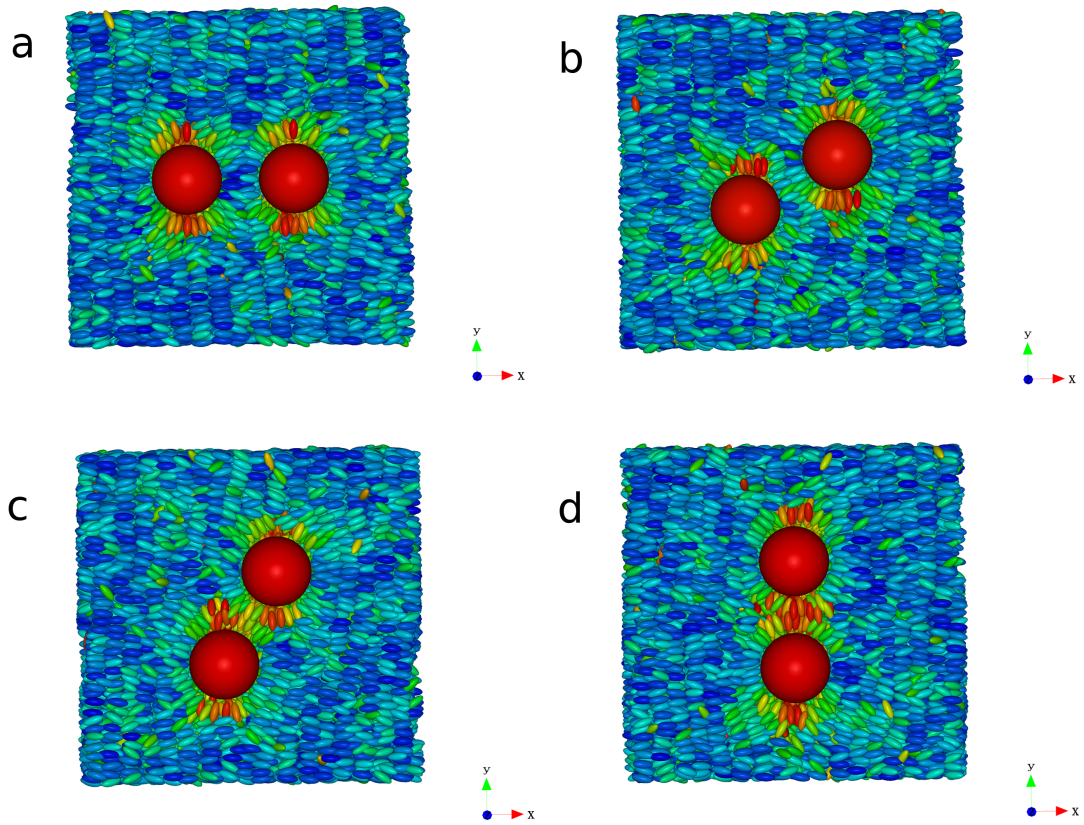

Figure 7.20: Visualizations of final configurations for systems with $N = 25000$ LC particles and fixed colloid pairs with homeotropic surface anchoring at different angles ϕ: (a) $\phi = 00°$, (b) $\phi = 30°$, (c) $\phi = 60°$, (d) $\phi = 90°$. The color of the particles indicates the deviation of its orientation from the global director $\hat{\mathbf{n}}_0$ in the system, dark blue meaning perfect alignment with $\hat{\mathbf{n}}_0$ and red meaning orthogonality with respect to $\hat{\mathbf{n}}_0$.

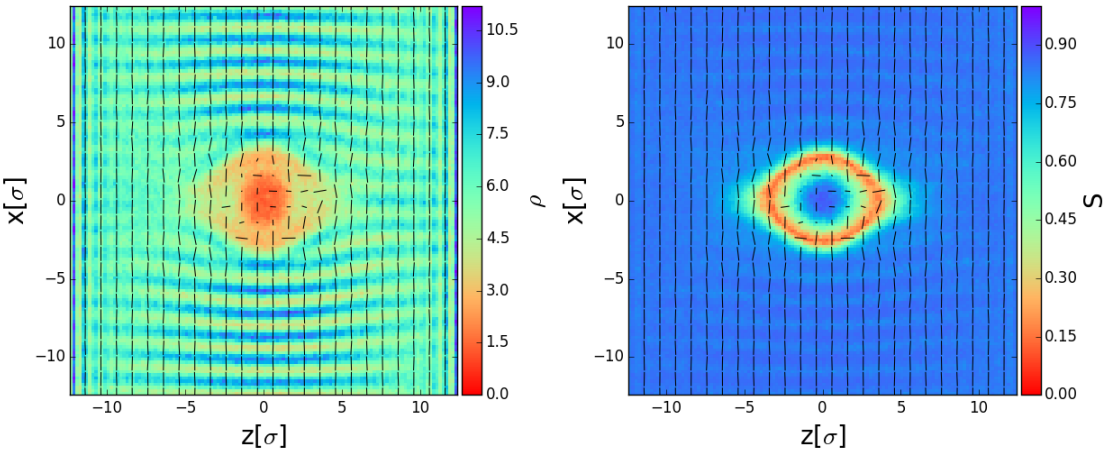

Figure 7.21: Cross section through the z-x-plane between both colloid, where the third defect ring forms. Note that the defect structure is not really circular but it is rather eliptical or lenticular.

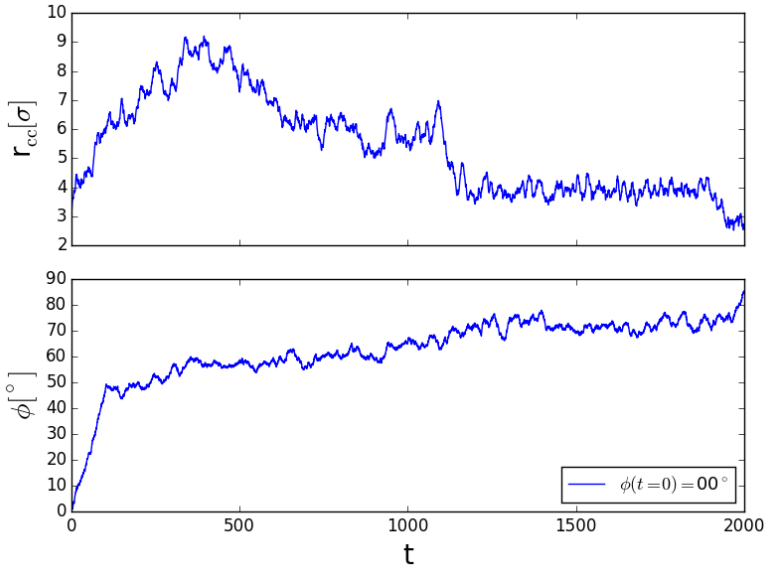

Figure 7.22: Time evolution of inter-colloid distance r_{cc} and angles ϕ, for a pair of colloid starting from $r_{\mathrm{cc}}(t=0) = 3\sigma$ and $\phi(t=0) = 0°$.

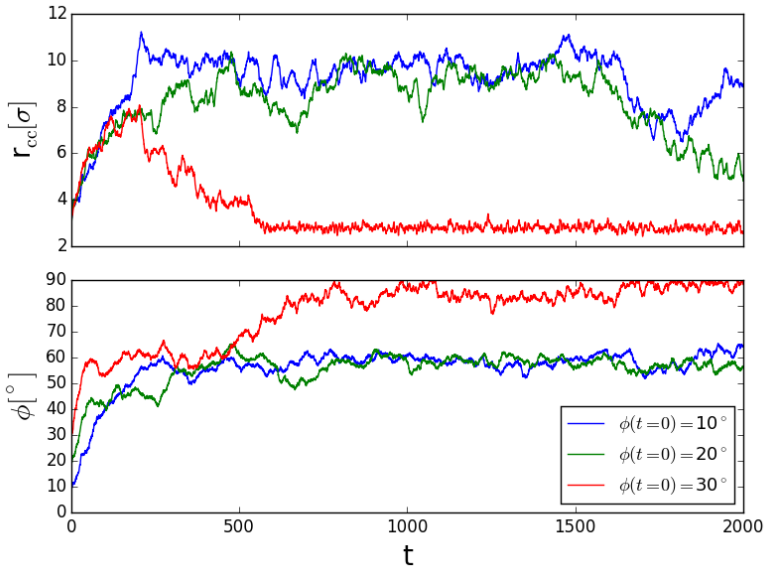

Figure 7.23: Time evolution of inter-colloid distance r_{cc} and angles ϕ, for pairs of colloid starting from $\phi(t=0) = 40°$, $\phi(t=0) = 50°$, $\phi(t=0) = 60°$. All pairs start from an inter-colloid distance $r_{cc}(t=0) = 3\sigma$.

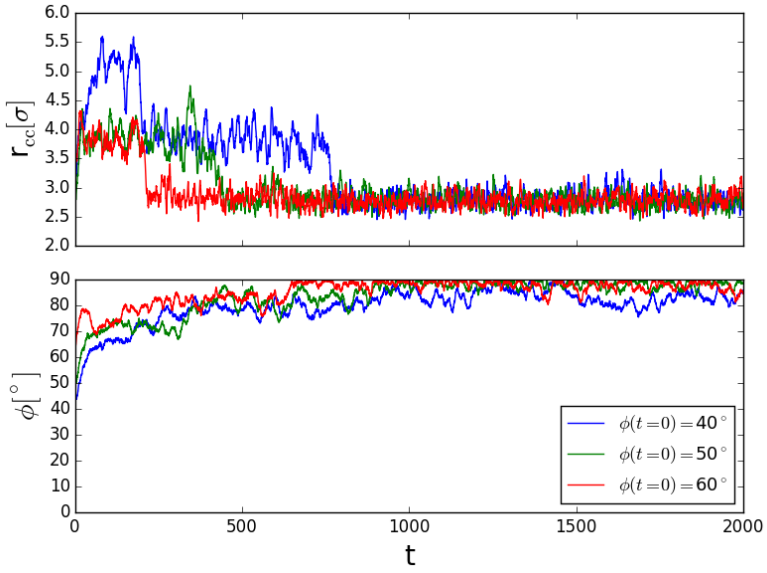

Figure 7.24: Time evolution of inter-colloid distance r_{cc} and angles ϕ, for pairs of colloid starting from $\phi(t=0) = 40°$, $\phi(t=0) = 50°$, $\phi(t=0) = 60°$. All pairs start from an inter-colloid distance $r_{cc}(t=0) = 3\sigma$.

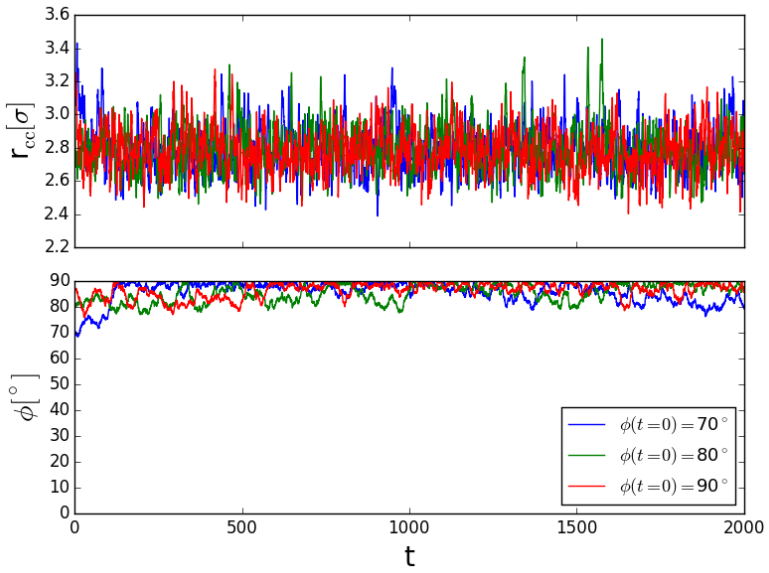

Figure 7.25: Time evolution of inter-colloid distance r_{cc} and angles ϕ, for a pair of colloid starting from $r_{\mathrm{cc}}(t=0) = 3\sigma$ and $\phi(t=0) = 0°$.

Bibliography

[1] P.-G. de Gennes and J. Prost, Oxford University Press, USA , 0 (1995).

[2] S. Sato, Optical Review **6**, 471 (1999).

[3] Y. Sato, T.-a. Tanaka, H. Kobayashi, K. Aoki, H. Watanabe, H. Takeshita, Y. Ouchi, H. Takezoe, and A. Fukuda, Japanese Journal of Applied Physics **28**, L483 (1989).

[4] K. Dolgaleva, S. K. Wei, S. G. Lukishova, S. H. Chen, K. Schwertz, and R. W. Boyd, JOSA B **25**, 1496 (2008).

[5] H. Stark, Physics Reports **351**, 387 (2001).

[6] K. Zuhail, P. Sathyanarayana, D. Seč, S. Čopar, M. Škarabot, I. Muševič, and S. Dhara, Physical Review E **91**, 030501 (2015).

[7] I. Muševič, M. Škarabot, U. Tkalec, M. Ravnik, and S. Žumer, Science **313**, 954 (2006).

[8] A. Nych, U. Ognysta, M. Škarabot, M. Ravnik, S. Žumer, and I. Muševič, Nature Communications **4**, 1489 (2013).

[9] N. Madhusudana and R. Pratibha, Molecular Crystals and Liquid Crystals **89**, 249 (1982).

[10] C. V. Yelamaggad, G. Shanker, U. S. Hiremath, and S. K. Prasad, Journal of Materials Chemistry **18**, 2927 (2008).

[11] J. D. Martin, C. L. Keary, T. A. Thornton, M. P. Novotnak, J. W. Knutson, and J. C. Folmer, Nature Materials **5**, 271 (2006).

[12] L. Onsager, Annals of the New York Academy of Sciences **51**, 627 (1949).

[13] M. A. Bates and D. Frenkel, The Journal of Chemical Physics **112**, 10034 (2000).

[14] N. D. Mermin, Reviews of Modern Physics **51**, 591 (1979).

[15] L. Giomi, M. J. Bowick, X. Ma, and M. C. Marchetti, Physical Review Letters **110**, 228101 (2013).

[16] S. Püschel-Schlotthauer, T. Stieger, M. Melle, M. G. Mazza, and M. Schoen, Soft Matter **12**, 469 (2016).

[17] E. Pouget, E. Grelet, and M. P. Lettinga, Physical Review E **84**, 041704 (2011).

[18] G. P. Alexander, B. G.-g. Chen, E. A. Matsumoto, and R. D. Kamien, Physical Review Letters **104**, 257802 (2010).

[19] G. Chahine, A. V. Kityk, K. Knorr, R. Lefort, M. Guendouz, D. Morineau, and P. Huber, Physical Review E **81**, 031703 (2010).

[20] D. B. Liarte, M. Bierbaum, R. A. Mosna, R. D. Kamien, and J. P. Sethna, Physical Review Letters **116**, 147802 (2016).

[21] K. Zuhail, S. Čopar, I. Muševič, and S. Dhara, Physical Review E **92**, 052501 (2015).

[22] K. Zuhail and S. Dhara, Applied Physics Letters **106**, 211901 (2015).

[23] L. Landau, Phys. Z. Sowjetunion **11**, 26 (1937).

[24] Z. X. Fan and W. Haase, The Journal of Chemical Physics **95**, 6066 (1991).

[25] S. Hess and B. Su, Zeitschrift für Naturforschung A **54**, 559 (1999).

[26] J. Lennard and I. Jones, in *Proc. R. Soc. London*, Vol. 106 (1924) pp. 441–477.

[27] S. Giura and M. Schoen, Physical Review E **90**, 022507 (2014).

[28] F. C. Frank, Discussions of the Faraday Society **25**, 19 (1958).

[29] P. J. Collings and M. Hird, *Introduction to liquid crystals: chemistry and physics* (CRC Press, 1997) Chap. 10.3, pp. 202–210.

[30] M. P. Allen and D. Frenkel, Physical Review A **37**, 1813 (1988).

[31] M. P. Allen and D. Frenkel, Physical Review A **42**, 3641 (1990).

[32] P. Poulin and D. Weitz, Physical Review E **57**, 626 (1998).

[33] O. Lavrentovich, Liquid crystals **24**, 117 (1998).

[34] N. Mermin, in *Quantum fluids and solids* (Springer, 1977) pp. 3–22.

[35] L. Carroll, *The hunting of the snark: an agony in eight fits* (Xist Publishing, 2016).

[36] J. M. Ilnytskyi and M. R. Wilson, Computer Physics Communications **148**, 43 (2002).

[37] S. Nosé, Molecular Physics **52**, 255 (1984).

[38] W. G. Hoover, Physical Review A **31**, 1695 (1985).

[39] W. G. Hoover, Physical Review A **34**, 2499 (1986).

[40] E. Hairer, C. Lubich, G. Wanner, *et al.*, Acta Numerica **12**, 399 (2003).

[41] D. Tildesley and M. Allen, Clarendon, Oxford (1987).

[42] R. D. Skeel, G. Zhang, and T. Schlick, SIAM Journal on Scientific Computing **18**, 203 (1997).

[43] M. P. Allen and D. J. Tildesley, *Computer simulation of liquids* (Oxford university press, 1989).

[44] J. Muller, N. Brisebarre, F. de Dinechin, C. Jeannerod, V. Lefèvre, G. Melquiond, N. Revol, D. Stehlé, and S. Torres, *Handbook of Floating-Point Arithmetic* (Birkhäuser Boston, 2009).

[45] S. Püschel-Schlotthauer, V. Meiwes Turrión, T. Stieger, R. Grotjahn, C. K. Hall, M. G. Mazza, and M. Schoen, The Journal of Chemical Physics **145**, 164903 (2016).

[46] M. Cifelli and C. Veracini, Molecular Crystals and Liquid Crystals **576**, 127 (2013).

[47] D. Andrienko, G. Germano, and M. P. Allen, Physical Review E **63**, 041701 (2001).

[48] M. Melle, S. Schlotthauer, M. G. Mazza, S. H. Klapp, and M. Schoen, The Journal of Chemical Physics **136**, 194703 (2012).

[49] O. Diat, D. Roux, and F. Nallet, Journal de Physique II **3**, 1427 (1993).

[50] D. Roux, F. Nallet, and O. Diat, EPL (Europhysics Letters) **24**, 53 (1993).

[51] M. C. Choi, T. Pfohl, Z. Wen, Y. Li, M. W. Kim, J. N. Israelachvili, and C. R. Safinya, Proceedings of the National Academy of Sciences USA **101**, 17340 (2004).

[52] M. Conradi, M. Ravnik, M. Bele, M. Zorko, S. Žumer, and I. Muševič, Soft Matter **5**, 3905 (2009).

[53] E. Harzheim, *Einführung in die kombinatorische Topologie* (Wiss. Buchges., 1978) pp. 176–177.

[54] O. Guzmán, E. Kim, S. Grollau, N. Abbott, and J. de Pablo, Physical Review Letters **91**, 235507 (2003).

[55] S. Čopar, Physics Reports **538**, 1 (2014).

Erklärung nach §18(8) der Prüfungsordnung für den Bachelor-Studiengang Physik und den Master-Studiengang Physik an der Universität Göttingen:

Hiermit erkläre ich, dass ich diese Abschlussarbeit selbständig verfasst habe, keine anderen als die angegebenen Quellen und Hilfsmittel benutzt habe und alle Stellen, die wörtlich oder sinngemäß aus veröffentlichten Schriften entnommen wurden, als solche kenntlich gemacht habe.
Darüberhinaus erkläre ich, dass diese Abschlussarbeit nicht, auch nicht auszugsweise, im Rahmen einer nichtbestandenen Prüfung an dieser oder einer anderen Hochschule eingereicht wurde.

Göttingen, den November 21, 2016

(Victor Meiwes Turrión)